UCSF
UC San Francisco Previously Published Works

Title

The ~1.4 Ga A-type granitoids in the "Chottanagpur crustal block" (India), and its relocation from Columbia to Rodinia?

Permalink

Journal

ISSN

Authors

Sequeira, Nicole
Bhattacharya, Abhijit
Bell, Elizabeth

Publication Date

DOI

Peer reviewed

Research Paper

The ~1.4 Ga A-type granitoids in the "Chottanagpur crustal block" (India), and its relocation from Columbia to Rodinia?

Nicole Sequeira [a,c,*], Abhijit Bhattacharya [a], Elizabeth Bell [b]

[a] *Department of Geology and Geophysics, Indian Institute of Technology, Kharagpur 721 302, India*
[b] *Department of Earth, Planetary and Space Sciences, University of California, 595 Charles Young Drive East, Los Angeles, CA 90095-1567, USA*
[c] *School of Earth, Ocean and Atmospheric Sciences, Goa University, Taleigao, Goa 403516, India*

ARTICLE INFO

ABSTRACT

In paleogeographic reconstructions of the Columbia and Rodinia Supercontinents, the position of the Greater India landmass is ambiguous. This, coupled with a limited understanding of the tectonic evolution of the mobile belts along which the mosaic of crustal domains in India accreted, impedes precise correlation among the dispersed crustal fragments in supercontinent reconstructions. Using structural, metamorphic phase equilibria, chronological and geochemical investigations, this study aims to reconstruct the tectonic evolution of the Chottanagpur Gneiss Complex (CGC) as a distinct crustal block at the eastern end of the Greater Indian Proterozoic Fold Belt (GIPFOB) along which the North India Block (NIB) and the South India Block (SIB) accreted. The study focuses on two issues, e.g. dating the Early Neoproterozoic (0.92 Ga) accretion of the CGC with the NIB contemporaneous with the assembly of Rodinia, and documenting the widespread (>24,000 km^2) plutonism of 1.5–1.4 Ga weakly peraluminous, calc-alkalic to alkali-calcic and ferran A-type granitoids (± garnet) devoid of mafic microgrannular enclaves and coeval mafic emplacements in the crustal block. These dominantly within-plate granitoids arguably formed by asthenospheric upwelling induced partial melting of garnet-bearing anatectic quartzofeldspathic gneisses that dominate the Early Mesoproterozoic basement of the block. The major and trace element chemistry of the granitoids is similar to the 1.35–1.45 Ga A-type granitoids in Laurentia/Amazonia emplaced contemporaneous with the 1.5–1.3 Ga breakup of the Columbia Supercontinent. This study suggests the Chottanagpur Gneiss Complex occured as a fragmented crustal block following the breakup of the Columbia Supercontinent; the crustal block was subsequently integrated within India during the Early Neoproterozoic oblique accretion between the NIB and SIB contemporaneous with the Rodinia Supercontinent assembly.

1. Introduction

The Greater India landmass is a mosaic of Archean crustal domains that were accreted along Late Archean through Proterozoic to Early Paleozoic mobile belts (Fig. 1; Radhakrishna and Naqvi, 1986). The accretion between the Western Dharwar and the Eastern Dharwar Cratons (Fig. 1) is the oldest 2.55–2.51 Ga (Manikyamba and Kerrich, 2011, and references therein), whereas the youngest accretion zones formed as late as ~500 Ma, e.g. along the western margin of the Eastern Ghats Province (Nasipuri et al., 2018), the Achankovil Shear Zone between the Trivandrum and the Madurai Blocks in the Kerala Khondalite Belt, at the southern tip of India (Santosh et al., 2006), and in the Shillong-Meghalaya Gneiss Complex (Chatterjee et al., 2007) (Fig. 1). As the final configuration of the Greater Indian landmass possibly came into existence as late as ~500 Ma, the paleogeographic positions of the

Greater Indian landmass in the reconstructions of the Paleoproterozoic Columbia Supercontinent (Rogers and Santosh, 2002; Evans and Mitchell, 2011; Meert and Santosh, 2017) and the Late Mesoproterozoic to Early Neoproterozoic Rodinia Supercontinent (McMenamin and McMenamin, 1990; Li et al., 2008; Evans, 2009) are enigmatic.

Based on paleomagnetic data in the Paleoproterozoic dykes (2.37–1.88 Ga) of the Dharwar, Bundelkhand and Bastar cratons (Fig. 1) (Halls et al., 2007; Pradhan et al., 2012; Meert et al., 2013; Belica et al., 2014; Nagaraju et al., 2018; Pivarunasa et al., 2019), India is assigned peripheral positions in most reconstructions of the Columbia Supercontinent; others suggest India was not a part of the Columbia Supercontinent (Zhao et al., 2004; Li et al., 2008). On the other hand, paleomagnetic studies pertaining to the formation and breakup of the Rodinia Supercontinent are obtained from the Neoproterozoic dykes (1.2–0.75 Ga) in the Dharwar craton (Miller and Hargraves, 1994; Radhakrishnan and Mathew, 1996; Pradhan et al., 2008) and Bundelkhand craton (Pradhan et al., 2012), Vindhyan sediments (Gregory et al., 2006; Malone et al., 2008) and the Malani Igneous
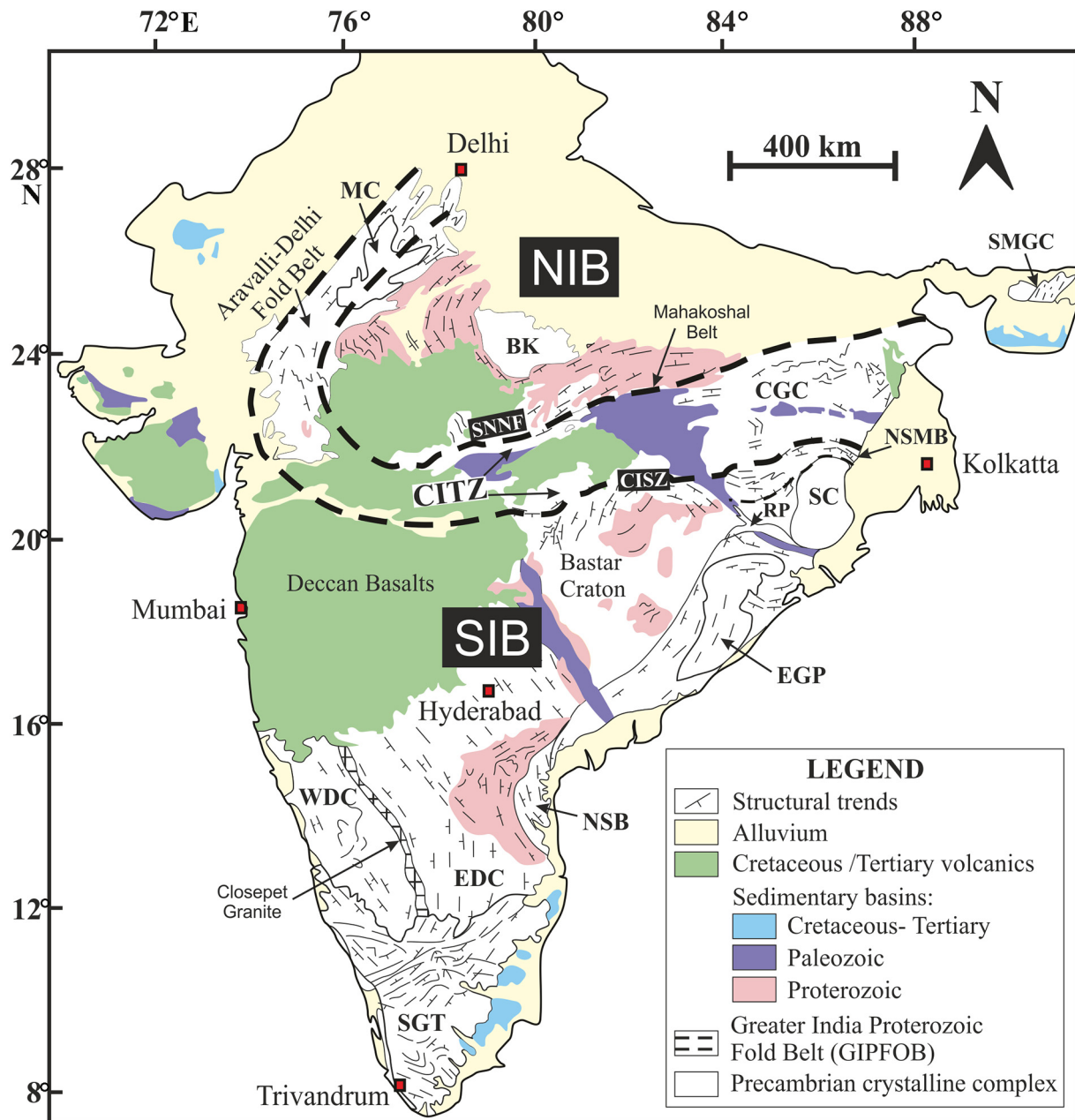
Fig. 1. Tectonic domains of peninsular India (modified after Prabhakar et al., 2014). The Greater India Proterozoic Fold Belt (GIPFOB) is marked by the thick dashed lines. Acronyms used: MC: Mewar Craton, BK: Bundelkhand Craton, CITZ: Central Indian Tectonic Zone, CGC: Chottanagpur Gneiss Complex, SMGC: Shillong-Meghalaya Gneiss Complex, NSMB: North Singhbhum Mobile Belt, SC: Singhbhum Craton, RP: Rengali Province, EGP: Eastern Ghats Province, NSB: Nellore Schist Belt, WDC: Western Dharwar Craton, EDC: Eastern Dharwar Craton, SGT: Southern Granulite Terrain, SNNF: Son Narmada North Fault, CISZ: Central Indian Shear Zone.

Suite (Torsvik et al., 2001; Gregory et al., 2009; Meert et al., 2013). However, as the Indian landmass grew due to accretion of smaller crustal blocks through time, the paleomagnetic pole data used to ascertain the position of India within the Proterozoic Supercontinents applies only to the particular crustal domain/craton from which the paleopole is derived, and not to the entire Indian landmass, for the entire landmass may not have existed at that point of time.

Paleomagnetic data in the intervening time span (1.9–1.2 Ga) is lacking in India, the only exception being the paleomagnetic pole calculated by Pisarevskiy et al. (2013) from the localized arc-related Lakhna dykes (1.47 Ga) in the Bastar Craton (Fig. 1) that places SE India close to Baltica in the Mid-Mesoproterozoic. Baltica, Laurentia and Amazonia formed the core of the Columbia Supercontinent

(Rogers and Santosh, 2002, 2009; Zhao et al., 2004; Li et al., 2008; Pisarevskiy et al., 2013). The age is significant because it is contemporaneous with the age of the fragmentation of the Columbia Supercontinent (1.5–1.35 Ga; Condie, 2002; Zhao et al., 2004; Rogers and Santosh, 2009; Pisarevskiy et al., 2013). Asthenosphere upwelling and plume-driven occurrences of globally widespread emplacement of anorogenic granitoids, coeval rhyolite and mafic volcanism, and rift-related ensialic sedimentation in Laurentia, Baltica, Amazonia, Tanzania and Congo, the Siberian Craton and the South China Craton (Rogers and Santosh, 2002, 2009; Zhao et al., 2004; Pisarevskiy et al., 2013; Han et al., 2017; Meert and Santosh, 2017) are cited as evidences for the breakup of the Columbia Supercontinent. However the 1.5–1.4 Ga ferroan A-type granitoids in the Rocky Mountains in

a magmatic belt >1000 km wide are possibly not associated with rifting in spite of the local occurrences of *syn*-plutonic extensional fabrics (Nyman et al., 1994; Ferguson et al., 2004 and references therein). Hoffman (1989) suggested that the anorthosite-ferrogranite suites extending NW from California to Quebec were produced by mantle upwelling, without rifting. Also there is little evidence of *syn*-rift sediments (although the Belt Supergroup in British

Columbia, Montana and Idaho formed by rifting at this age; Evans et al., 2000), and dike swarms of this age are lacking in the western US.

In the Greater India Landmass, ~1.4 ± 0.1 Ga magmatism is largely unknown, except for the ~1.4 Ga silica under-saturated syenite complexes (Kumar et al., 2007), the Elchuru alkaline rocks (1442 ± 30 Ma; Upadhyay et al., 2006) of the Eastern Ghats Mobile Belt at the
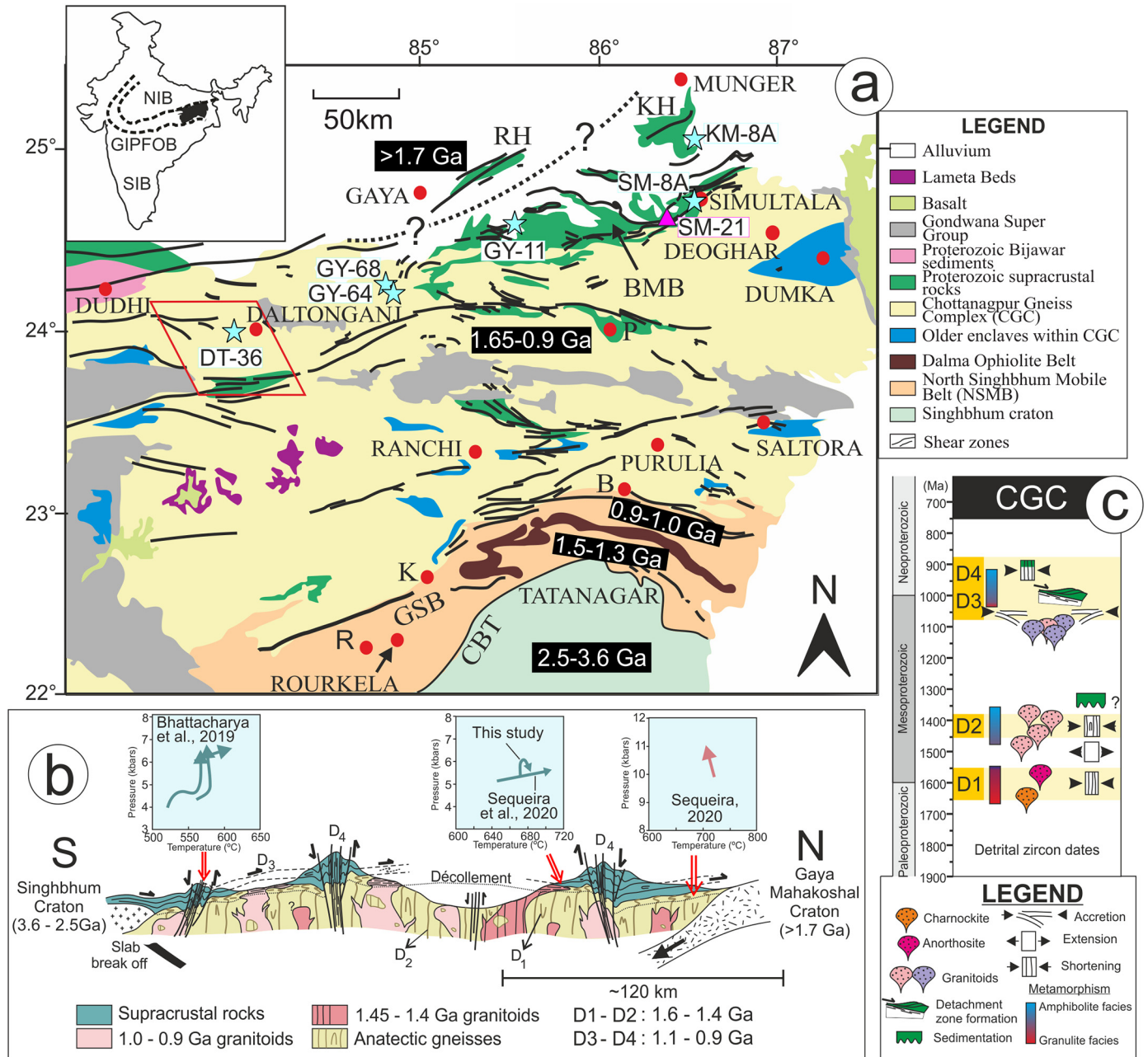

Fig. 2. (a) Simplified geological map of the CGC showing the network of E-striking shear zones (dark lines), locations of the zircon dated samples (stars) and sample SM21 used in P-T pseudosection construction (pink triangle). The southern terrane boundary shear zone in the CGC is indicated by the line straddling R (Rajgangpur), K (Kolomda) and B (Balarampur); the poorly constrained northern terrane boundary is shown by broken line south of Gaya. The Dalma Ophiolite Belt (DOB) demarcates the boundary between the Grenvillian-age North-NSMB and the Mesoproterozoic South-NSMB (Mahato et al., 2008). The Dalma Ophiolite Belt (DOB) demarcates the boundary between the Grenvillian-age North-NSMB and the Mesoproterozoic South-NSMB (Mahato et al., 2008; Rekha et al., 2011). The Bihar Mica Belt (BMB) and the Gangpur Schist Belt (GSB) are shown. RH and KH stand for Rajgir Hills and the Kharagpur Hills. Locations cited in text are indicated. The broad age ranges in different crustal domains are indicated in black boxes: Singhbhum craton (Prabhakar and Bhattacharya, 2013), NSMB (Mahato et al., 2008; Rekha et al., 2011), CGC (this study and references therein), Gaya-Rajgir crustal domain (Chatterjee and Ghose, 2011; Saikia et al., 2017). The inset is a map of India showing the Greater India Proterozoic Fold Belt (GIPFOB; broken line) sandwiched between the North India Block (NIB) and the South India Block (SIB), with the CGC (darkened) at its eastern end. The red box denotes the area structurally mapped in Fig. 5. (b) Schematic geologic section across the CGC summarizes the mesoscale structures, lithologies and ages in the CGC based on recent findings (see text for discussion). Also included are the reconstructed P-T paths in supracrustal rocks at the southern margin (Bhattacharya et al., 2019), the centrally-located areas (Sequeira et al., 2020), and in the anatectic granitoid GY-68 at the northern margin (Sequeira, 2020). (c) Time bar shows deformation episodes, metamorphic events and magmatic emplacements in the CGC. For details refer text. Note the bar diagram is based on the findings in this study.

southeastern tip of the Eastern Ghats Granulite Belt (Fig. 1), and the reports of Chatterjee et al. (2007) of ~1.4 Ga monazite chemical dates of unknown origin. Mukherjee et al. (2017, 2018a, 2019) reported 1.45 Ga A-type granitoids in the Dumka-Deoghar sector in the Chottanagpur Gneiss Complex (CGC), at the eastern end of the Greater India Proterozoic Fold Belt (GIPFOB, Fig. 1; Radhakrishna and Naqvi, 1986) which is inferred to be the zone of amalgamation of the North India Block (NIB) and the South India Block (SIB) (Fig. 1).

This study for the first time documents the widespread occurrence of the Mid-Mesoproterozoic A-type ferroan granite plutonism in an extensional tectonic setting in the CGC. The CGC covers an area > 80,000 km^2 in Eastern India (Fig. 2a), but the structural and lithological continuity across the terrain has thus far not been explored. Detailed analyses of mesoscale structures in the western part of the CGC, new metamorphic P-T path reconstruction in north-CGC, and new monazite chemical dates and U-Pb zircon dates are integrated with existing data elsewhere in the CGC to suggest a coherent tectonic evolutionary history for the entire crustal block of the CGC. It is suggested that the CGC crustal block is a fragment of the Columbia Supercontinent that was integrated within India during the oblique Early Neoproterozoic accretion between the NIB and the SIB, contemporaneous with the Rodinia Supercontinent assembly (Sequeira and Bhattacharya, 2020; Sequeira et al., 2020, and references therein).

2. A synthesis of the tectonics in the CGC

The Precambrian crystalline rocks of the CGC (Fig. 2a) may be grouped into three lithodemic units: (a) The Early Mesoproterozoic (1.7–1.5 Ga: Acharyya, 2003; Karmakar et al., 2011; Rekha et al., 2011; Mukherjee et al., 2017, 2019) granulite facies anatectic felsic orthogneisses, charnockites, garnet–sillimanite–K-feldspar metapelites, calc-silicate gneisses, mafic granulites, and lens-shaped plutons of massif anorthosites (1.5 Ga; Chatterjee et al., 2008) and syenites; (b) the Mid-Mesoproterozoic granitoids (1.45 Ga; Mukherjee et al., 2017, 2018a, 2019) (earlier restricted to the Dumka-Deoghar area), and expansive Late Mesoproterozoic to Early Neoproterozoic granitoids (Karmakar et al., 2011; Rekha et al., 2011; Bhattacharya et al., 2016, 2019; Sequeira and Bhattacharya, 2020, 2021; Sequeira et al., 2020); and (c) linear belts of allochthonous (Sequeira and Bhattacharya, 2020, 2021; Sequeira et al., 2020) non-anatectic amphibolite facies supracrustal rocks composed of muscovite-biotite $\pm$ garnet $\pm$ sillimanite schists, epidote-amphibole-plagioclase bearing meta-marls, meta-dolomites and amphibolites. The supracrustal rocks are closely associated with a network of steeply-dipping, dominantly left-lateral curvilinear E/ESE/ENE-striking transpressional shear zones (Fig. 2a) (Bhattacharya et al., 2019; Sequeira and Bhattacharya, 2020, 2021; Sequeira et al., 2020).

2.1. Structural and kinematic analysis

Based on structural analyses (Maji et al., 2008; Rekha et al., 2011; Bhattacharya et al., 2016, 2019; Sequeira and Bhattacharya, 2020, 2021; Sequeira et al., 2020) and deformation kinematics (Bhattacharya et al., 2019; Sequeira and Bhattacharya, 2020; Sequeira et al., 2020) four major deformation events (D1 to D4) are recognized in the central, southern and eastern parts of the CGC. Supplementary Figure 1 displays the field areas investigated in the previous studies that are pertinent in the present context. The schematic cross-section across the CGC (Fig. 2b) and a time-bar diagram showing the different geological events (Fig. 2c) are reconstructed based on synthesis of the earlier findings, and those presented in this study (see following text).

Only the Early Mesoproterozoic anatectic gneisses in the basement preserve the inter-relationship between the early D1 fabric (metatexite layering) and the later D2 foliations. Both the fabrics are steeply-dipping and N-trending, where unaffected by the subsequent D3 and D4 deformations. Intrafolial to the penetrative D2 fabric, rootless hinges of steep to moderately plunging folds on early metatexite layers, and boudinaged metatexite layers, are the remnants of the oldest D1 deformation in the CGC. The Mid-Mesoproterozoic granitoids intrusive into the basement gneisses contain only the penetrative high-T D2 fabrics, but lack the intrafolial folds on D1 layers. Syn-D2 anatexis manifested by diatexite pods at boudin necks is uncommon, and evidence for post-D2 melting in the gneisses is lacking (Sequeira et al., 2020). Granitoids lacking both the D1 and D2 fabrics occur as stocks and bosses within the basement rocks.

At structurally higher levels, the basement rocks evolve into a carapace of flat-lying to shallow-dipping granitoid mylonites and non-anatectic amphibolite facies supracrustal rocks inter-leaved with recumbent to gently inclined folds on the D1-D2 composite fabric in the anatectic basement gneisses (D3 deformation; Sequeira and Bhattacharya, 2020; Sequeira et al., 2020). Relict intrafolial folds in the supracrustal rocks are obliterated, but early metamorphic fabrics are preserved as oblique strands in D3 intrafolial domains, and as inclusion trails in pre-D3 garnet porphyroblasts in biotite-muscovite schists (Bhattacharya et al., 2019; Sequeira et al., 2020). The supracrustal rocks in the shallow-dipping carapace are inferred to be an allochthonous unit (Bhattacharya et al., 2016, 2019; Sequeira and Bhattacharya, 2020, 2021; Sequeira et al., 2020), and the carapace is regionally expansive in crustal sections that are not deeply eroded. Kinematic analyses indicate the shallowly-dipping mylonitic fabric in the granitoids in eastern CGC (Sequeira et al., 2020) is a pure shear dominated extensional fabric.

The D4 deformation is manifested by networks of anastomosing ESE to ENE-striking regional scale steeply-dipping shear zones that modify both the steeply-dipping basement gneisses unaffected by the D3 deformation, and the overlying shallowly-dipping D3 carapace (Bhattacharya et al., 2016, 2019; Sequeira and Bhattacharya, 2020, 2021; Sequeira et al., 2020). The pure shear dominated transpressive shear zones exhibit dominantly sinistral kinematics, although shorter shear zone segments with dextral kinematics have also been observed (Bhattacharya et al., 2019; Sequeira and Bhattacharya, 2020; Sequeira et al., 2020). In the Dumka-Deoghar-Giridih-Chakai segment in east-CGC (Supplementary Figure 1), these transpressive shear zones are associated with orogen-parallel inclined extrusion leading to metamorphic core complex formation (Sequeira et al., 2020). The variations in the stretching lineations in the D4 shear zones are caused by competency differences in the rocks, variations in the convergence angles during accretion (Sequeira and Bhattacharya, 2020), and the amount of triclinicity of the deformation strain (Sequeira and Bhattacharya, 2020; Sequeira et al., 2020).

The D3-D4 structures are attributed to Grenvillian-age oblique accretion of the CGC with the composite of the North Singhbhum Belt and the Singhbhum Craton along the southern margin of CGC (Rekha et al., 2011; Bhattacharya et al., 2016, 2019), and between the CGC and the Paleoproterozoic ensemble of granitoids and low-grade supracrustal rocks of the Gaya-Rajgir Belt along the northern margin of the CGC (Sequeira and Bhattacharya, 2021). The Gaya-Rajgir Belt shares considerable structural, lithological and chronological similarities with the Mahakoshal Belt further to the west along the strike extension of the Gaya-Rajgir Belt (Deshmukh et al., 2017; and references therein). The Grenvillian-age accretion at the southern margin of CGC initiated with northward subduction of the NSMB leading to profuse Grenvillian-age felsic magma emplacements within the CGC. Following slab break off, continued crustal convergence caused the metamorphosed orogenic wedge sediments and interleaved distended ultramafic slabs to be thrust northward (D3) over the CGC, post-dating solidification of the granitoids (Bhattacharya et al., 2019). With continued shortening these shallowly-dipping D3 fabrics were folded (D4) and dissected by orogen-parallel steeply-dipping D4 shear zones. At the northern boundary, both the Grenvillian-age D3 and D4 fabrics are

documented in the CGC; the CGC is thrust northwards over the Paleoproterozoic Gaya-Rajgir crustal block (Sequeira and Bhattacharya, 2021), but the transpressive steeply-dipping D4 shear zones are not prominent as in the south.

2.2. Thermo-barometric controls on deformation events in the CGC

Fig. 3 provides a summary of existing metamorphic P-T paths retrieved for the Early Mesoproterozoic basement gneisses, and the overlying Early Neoproterozoic supracrustal rocks and a granitoid in the shallowly-dipping carapace; the P-T path retrieved in this study is also shown. Along the accretion margins, the metamorphic P-T paths in the supracrustal rocks exhibit near-isothermal loading, e.g. 500–550 °C, 5–7 kbar (Bhattacharya et al., 2019) at the southern margin (Figs. 2b and 3), and 700–720 °C, 9.5–11 kbar (Sequeira, 2020) at the northern margin (Figs. 2b and 3). At the southern margin, the loading paths are punctuated by heating segments inferred by Bhattacharya et al. (2019) (Fig. 3). At the northern margin, loading induced in situ melting in the shallowly-dipping anatectic granitoid (Fig. 4a) (GY-68; Sequeira, 2020) is synchronous with thrusting of the CGC over the Paleoproterozoic undeformed granitoids (Fig. 4b; Chatterjee and Ghose, 2011; Saikia et al., 2017) and greenschist to sub-greenschist facies rocks of the Gaya-Mahakoshal Belt (Sarkar and Basu Mallick, 1982; Deshmukh et al., 2017; Sequeira and Bhattacharya, 2021). In the centrally-located parts of the CGC, a garnet-bearing muscovite-biotite-sillimanite schist in the shallowly-dipping carapace yields an Early Neoproterozoic mid-crustal prograde heating path (5–6 kbar; 620–680 °C; Sequeira et al., 2020; Figs. 2b and 3).
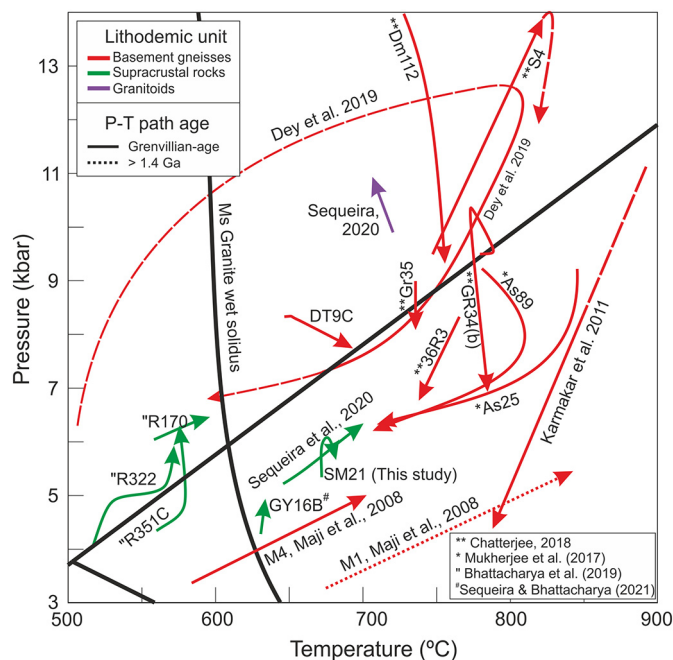

Fig. 3. Summary of existing P-T paths reconstructed in different parts of the CGC. The P-T loci of the wet melting curve for granite and the phase transitions of kyanite-sillimanite and sillimanite-andalusite are for reference only. The continuous lines are Early Neoproterozoic paths, and the dotted lines are >1.4 Ga, as suggested by the original authors. The broken sectors of the P-T paths are suggested by the original authors. The P-T paths shown in green are for muscovite-biotite (± garnet ± staurolite) schists: samples prefixed with R are from the southern accretion zone (Bhattacharya et al., 2019), samples labeled SM-22 is from the east-central part of CGC (Sequeira et al., 2020); the P-T paths for muscovite-biotite-garnet schist SM-21 is from this study and GY-16B is after (Sequeira and Bhattacharya, 2021). P-T path in magenta is derived from an anatectic granitoid (GY-68B) at the northern accretion zone (Sequeira, 2020) and discussed in detail in this study.

These Early Neoproterozoic P-T paths obtained in the non-anatectic amphibolites facies supracrustal rocks sharply contrast with the granulite facies P-T paths obtained in the basement gneisses, e.g. felsic orthogneisses, mafic granulites and garnet-sillimanite gneisses in the basement (Fig. 3). The P-T paths in the basement gneisses exhibit varied trajectories, although clockwise P-T paths dominate (Karmakar et al., 2011; Mukherjee et al., 2017; Chatterjee et al., 2008; Dey et al., 2019). These paths exhibit pronounced decompression and cooling sectors in the retrograde sector (Fig. 3). An Early Neoproterozoic age is assigned to the retrograde P-T path in the multiply-deformed poly-metamorphic basement rock having polychronous (Early/Mid-Mesoproterozoic to Early Neoproterozoic) zircon grains, and in which the Early Neoproterozoic dates are obtained from discontinuous thin rims (few tens of microns wide) around the older zircon cores that constitute major parts of the zircon grains (Mukherjee et al., 2017, 2019; Dey et al., 2019). Two aspects are noteworthy. First, the authors do not document the D3-D4 deformations (Sequeira et al., 2020) in the rocks around Dumka-Deogarh, and do not assess their impact in the P-T path reconstructions. Second, the high-T decompression-cooling sector is incompatible with the P-T trajectories in the Early Neoproterozoic supracrustal rocks (Sequeira et al., 2020) that did not experience the Early Mesoproterozoic granulite facies metamorphism (Fig. 3). It is possible that the low-T Early Neoproterozoic imprint was not recorded in the basement gneisses because of their anhydrous nature. Also the basement rocks in the Dumka-Deogarh sector (Fig. 2a, Supplementary Figure 1) are located below the shallowly-dipping carapace (Sequeira et al., 2020), and therefore, were largely unaffected by the D3-D4 Early Neoproterozoic tectonism.

3. Additional structural and thermo-barometric constraints in the CGC

Most previous investigation have focused on the geochronologic and metamorphic aspects of the basement rocks of eastern and southern CGC (Karmakar et al., 2011; Rekha et al., 2011; Mukherjee et al., 2017, 2018a, 2018b, 2019; Dey et al., 2019). But the lithological-structural input to the tectonic history of the CGC has been sparse. Recent studies on the structural setup of the CGC show intrinsic similarities in southern, central and eastern CGC (Rekha et al., 2011; Bhattacharya et al., 2016, 2019; Sequeira and Bhattacharya, 2020, 2021; Sequeira et al., 2020), however, the continuity of these features into western CGC is largely unknown, although Patel et al. (2007) document locally developed structures in these areas. This study investigates a fairly large area in western CGC to establish the structural continuity of the CGC in the west, and to determine if the entire crustal block of the CGC behaved as a single coherently evolved crustal block.

3.1. The structural setup in western CGC

An area of ~2500 km² in the Daltongunj-Chipadohar sector was structurally mapped based on observations in 310 field stations (Fig. 5a; geologic section along A–A' in Fig. 5b). The area is divided into three sectors, e.g. *Sector A* comprises the steep-dipping (dip >70°) basement anatectic gneisses and foliated granitoids (Figs. 4c and 5a–c); *Sector B* is composed of flat/shallowly-dipping (dip amount < 40°) granitoid mylonites (Figs. 4d and 5a, b, d), and anatectic gneisses that exhibit gently-inclined and recumbent folds in (Figs. 4e and 5a, b, d); *Sector C* (dip amount: 41°–69°) is the transition zone where the NNW-trending steep foliations in Sector A are reoriented to the flat/shallow foliations in *Sector B* (Fig. 5a, b). The planar and linear structures in the three sectors are truncated by two E/ENE-trending steep-dipping sinistral shear zones that differ in their orientations of the stretching lineations, i.e. moderate/steep-plunging to the NNW in the northern shear zone (Fig. 5e), and gently plunging to the E and W in the southern shear zone (Figs. 4f and 5f). Supracrustal rocks in this
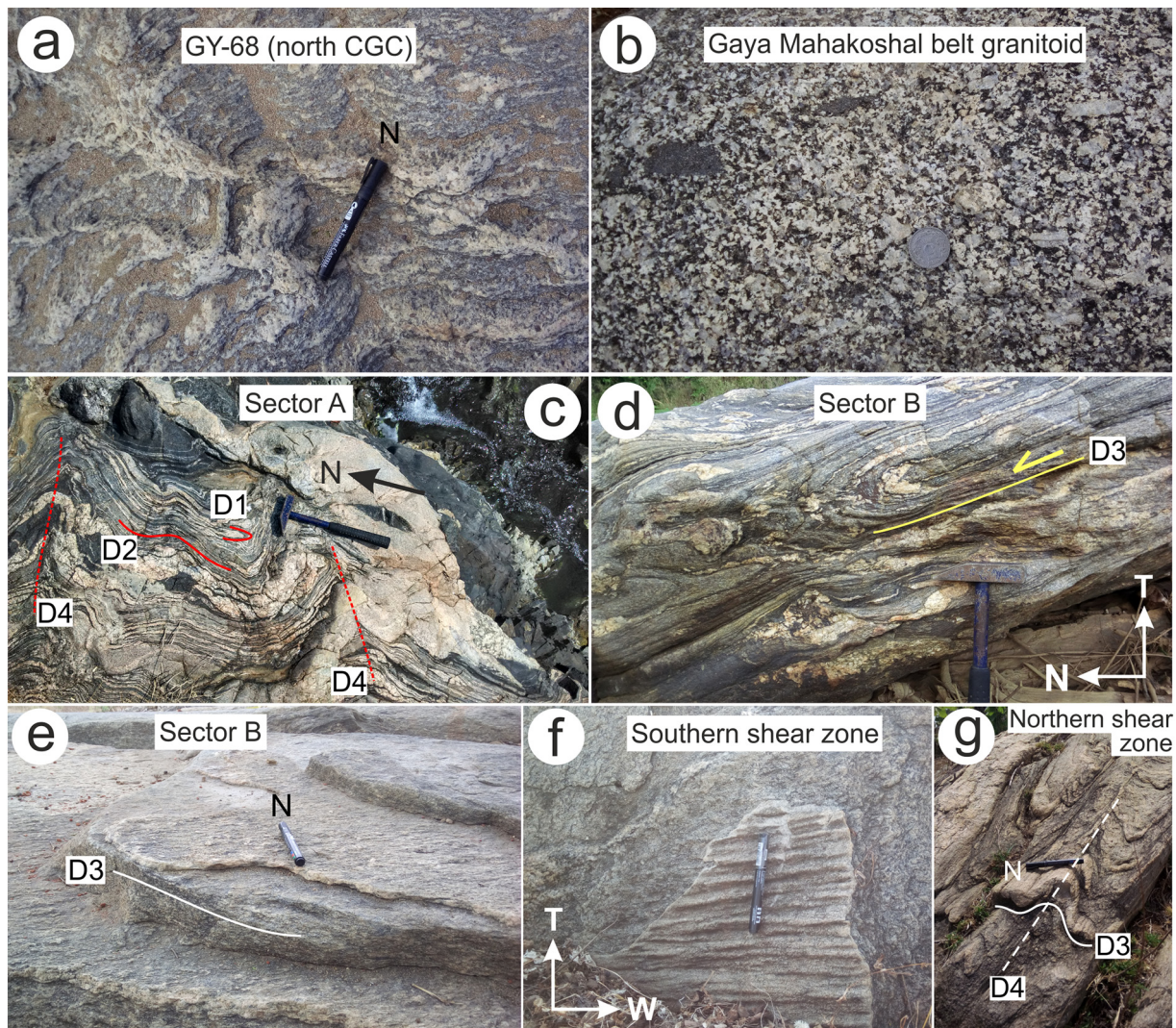
Fig. 4. Field photographs from the Gaya-Chatra area (a, b) and Daltongunj-Chipadohar area (c–g). (a) Plan view of shallowly-dipping (D3) anastomizing leucosome layers that coalesce into diatexite pods formed due to D3 thrusting in CGC anatectic granite mylonite (GY-68) close to the northern CGC margin. (b) Paleoproterozoic granitoid lacking penetrative mesoscale tectonic fabric. Note the randomly oriented nature of the euhedral feldspar phenocrysts, locally recrystallized (the coin is 2.5 cm in diameter). (c) Multiply-deformed steeply-dipping anatectic gneiss in Sector A (plan view) exhibit isoclinal D2 folds on D1 metatexite layers intrafolial to D2 fabrics, and open D4 folds with E-striking axial planes. (d) Section view (looking E) of gently inclined D3 folds and axial planes in anatectic gneisses in Sector B. Note the top-to-the-N shear sense. (e) Shallow-dipping granite mylonite with well-developed E-trending stretching lineation. (f) Steeply-dipping D4 granitoid mylonite with sub-horizontal stretching lineations. Crenulated quartz vein parallel to D4 foliation shows subhorizontal D4 fold hinges. (g) Perspective view (looking NE) showing gently-plunging non-cylindrical D4 folds on shallowly-dipping D3 layers in anatectic gneiss.

area are only preserved within the southern shear zone and are otherwise rare and highly weathered.

In *Sector A*, the steep NW/NNW-striking planar fabric (Fig. 5a, c) in the gneisses is identical to the penetrative D2 gneissic fabric documented in eastern CGC (Sequeira et al., 2020). It is axial planar to isoclinal steeply-plunging inclined and reclined intrafolial folds on garnet-bearing leucocratic layers (D1) (Fig. 4c). The Mid Mesoproterozoic granitoids (see section 4.2) intrusive into the gneisses also possess the N/NNW-striking D2 fabrics (Mukherjee et al., 2019), but the intrafolial D1 layers are lacking. However, some of these granitoids lack the steeply-dipping D2 fabric. By implication the emplacement of some of the Mid Mesoproterozoic granitoids was pre- to post-D2. The Late Mesoproterozoic/Early Neoproterozoic granitoids (section 4.1) intrude the basement gneisses post-D2. *Sector B* occurs in a 60 km long NW-trending belt and in two adjacent smaller domains (Fig. 5a). The shallow foliation (cf. Patel et al., 2007) in the granitoid mylonites and recumbent to gently-inclined folds and foliations in basement gneisses in this sector (Figs. 4d, e and 5d), identical to the D3 fabrics in other parts of the CGC, sharply

contrast with the steep-foliations in Sector A (Fig. 5c). The stretching lineations in Sector B granitoids plunge gently towards N/NW and E/ESE (Fig. 5a, d). *Sector C* (dip amount: 41°–69°) at the interface between Sector A and Sector B, therefore marks the lower boundary of a decollement in the basement gneisses of Daltongunj (Fig. 5b) overlain by the shallow-dipping D3 carapace. The shear zones (D4; cf. Sequeira et al., 2020) modify and truncate all earlier fabrics in the three lithodemic units. The axes of the D4 folds (Fig. 4g) in the carapace are collinear with the stretching lineations (Fig. 5e, f), but the D4 folds in the steeply-dipping basement gneisses underlying the carapace plunge steeply and the axial planes of D4 folds share a small angle obliquity with the D4 shears.

The four deformation events recorded in other parts of the CGC are therefore continuous into the Daltongunj-Chipadohar areas in western CGC and the carapace forming D3 translation tectonics appears to be a regional phenomenon that affected large parts of the CGC. The preservation of the shallow-dipping structures within the decollement transition zone depends on the present day level of the erosion surface and its intersection with the steep-to-shallow dipping transition zone.
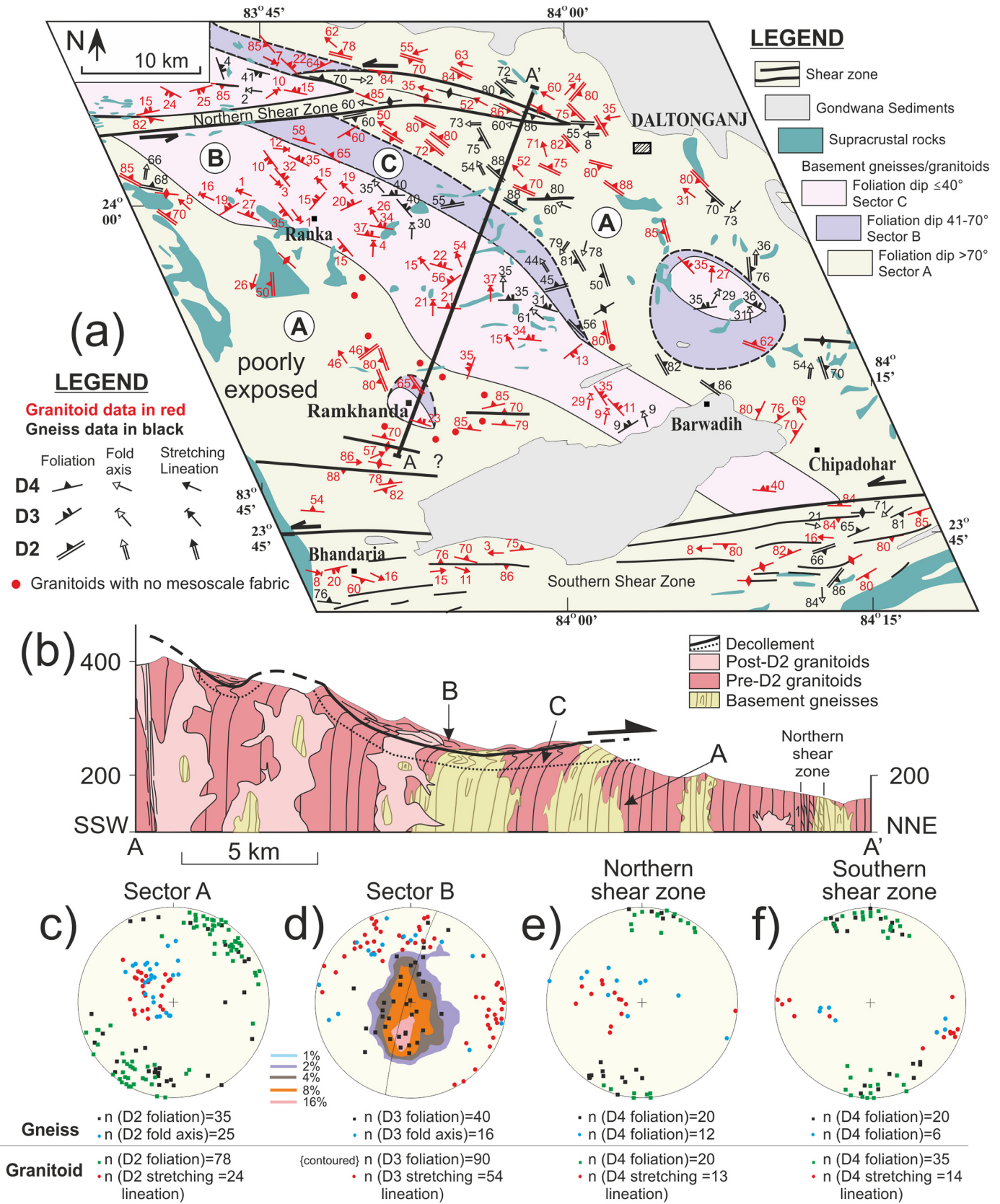
3.2. Metamorphic P-T conditions in the supracrustal unit in NE-CGC

In this section, we provide a new P-T path retrieved from a supracrustal rock located close to a D4 shear zone in north eastern CGC to understand the thermal response of the crust in response to the D3-D4 deformations. The rock is a quartz mica schist (SM-21) consisting of quartz, garnet, biotite, muscovite, K-feldspar, plagioclase and ilmenite in accessory amounts. The rock exhibits a penetrative shallowly-dipping D3 schistosity (Fig. 6a) defined by wisps of biotite-muscovite aggregates in a quart >> feldspar dominated matrix, with intrafolial folds on an earlier schistosity defined by the same minerals (Fig. 6a). The schistose layers occur in a mosaic of dynamically recrystallized grains of quartz pinned against the mica aggregates, and K-feldspar. The K-feldspar grains are chemically homogeneous, but some grains exhibit thin (<10 μm wide) plagioclase lamellae. Almost all plagioclases grains, xenomorphic in shape, occur adjacent to the significantly larger recrystallized K-feldspar grains. Ilmenite is the only Fe-Ti oxide mineral, largely restricted to the mica layers, and the modal abundance of ilmenite is <1%. Garnet porphyroblasts are sieve-textured with randomly oriented quartz inclusions, and occur as small (diameter < ~60 μm) discrete grains mostly within the quartz-feldspar matrix. The mica domains appear to terminate against the margins of the garnet grains, and thus the outer margins of the porphyroblasts seem to post-date D3 deformation.

The BSE image and the X-ray element maps for Fe, Mg, Mn and Ca of the analyzed garnet are shown in Fig. 6b. A core to rim profile of 602 μm (Fig. 6b) was chosen for the analyses; 72 spots within the garnet were analyzed for major element oxides. The profile was chosen to be distal from the biotite grain in contact to avoid retrograde Fe-Mg exchange between garnet and biotite. In addition, 26 spots were analyzed in muscovite, biotite and feldspars in the matrix (Supplementary Material 2).

The almandine-rich garnet exhibits weak nebulous chemical zoning. In Fig. 6c, $X_{Fe'}$ is computed as Fe/(Fe + Mg); and X_i [=i/(Mg + Fe + Ca + Mn)] where i = Fe, Mg, Mn and Ca. From the core to rim, X_{Ca} exhibits an overall increase, and then a rimward decrease; X_{Mn} shows a complementary trend, albeit weaker. X_{Mg} and X_{Fe} decrease weakly from core to the rim, but $X_{Fe'}$ shows almost no variation along the profile. Muscovite is near stoichiometric in composition; X_{Fe} [=Fe/(Fe + Mg)] in biotite varies between 0.78 and 0.79, and Ti contents in biotite are low, e.g. between 0.19 and 0.23 pfu (11 oxygens basis). Albite contents in plagioclase in both textural types vary between 61 and 67 mol% (Supplementary Material 2).

The bulk composition of the quartz-mica schist is approximated to the system $MnO–Na_2O–CaO–K_2O–FeO–MgO–Al_2O_3–SiO_2–H_2O$ (MnNCKFMASH). Perple_X_6.8.6 software version (Connolly, 2005) and the updated internally-consistent thermodynamic data set for end-member phase components (Holland and Powell, 1998) were used to construct the MnNCKFMASH P-T pseudosection (Fig. 6d). The following phases and the phase components (in square brackets) were chosen from those listed in the software: garnet, Gt [alm, py, gr, sps], staurolite, St [fst, mst, mnst], cordierite, Crd [crd, fcrd, hcrd, mncrd], biotite, Bio [ann, phl, east, mnbi], chlorite, Chl [ames, clin, daph, mnchl], Mica [mu, pa, cel, fcel], plagioclase, Pl [abh, an], K-feldspar, Kfs [san], clinozoisite [cz], andalusite [and], sillimanite [sill], kyanite [ky], epidote [ep] ilmenite, rutile and quartz [q]. The solution model of Holland and Powell (1998) is used for chlorite and staurolite.

Powell and Holland's (1999) model is used for biotite. The melt was modeled after Holland and Powell (2001) and White et al. (2001). The solution model CHA (Auzanneau et al., 2010; Coggon and Holland, 2002) is used for muscovite. Garnet was modeled using the Berman (1990) solution model. Quartz was taken to be in excess, and the fluid, assumed to be pure H_2O, was constrained by the loss on ignition (LOI) value in the computations.

None of the garnets in the sample display retrograde textures, hence the P-T path reconstructed here is considered to represent the growth history of the garnet. A clockwise P-T path was derived in the direction of increasing garnet volume percent, using the core to rim variations in X_{Fe}, X_{Mn}, X_{Ca} isopleths in the K-feldspar – plagioclase – biotite – muscovite – garnet–H_2O field of the pseudosection (Fig. 6d). The clockwise path involves a phase of near-isothermal loading, followed by heating along the hairpin bend and culminating with decompression-heating within a narrow temperature range, i.e. between 665 and 690 °C at mid-crustal depth. Thus the loading (D3) - decompression (D4) occurred in a relatively hot crust. In the absence of any immediate heat source, Bhattacharya et al. (2019) and Sequeira et al. (2020) suggest that the allochthonous supracrustal rocks were emplaced onto a relatively hot crust due to the release of heat from the profuse Early Neoproterozoic granitoid emplacements.

4. Geochronology

Age determination in monazites (Montel et al., 1996) using electron probe microanalyses is a low-cost method that can be employed to obtain robust dates. The blocking temperature of intra-crystalline U-Pb diffusion (> 800 °C) in monazite (Gardes et al., 2006) is comparable to that in zircon (Watson and Harrison, 1983), and therefore both monazites and zircons can be used to date high-T metamorphic and magmatic events. But unlike zircon, monazites experience grain-scale modifications in response to fluid-induced dissolution and re-precipitation (Poitrasson et al., 2000; Rasmussen and Muhling, 2007). Monazites can thus be used to date low-T metamorphic events as well, for which zircons may remain unresponsive. Since monazites readily modify chemically in polymetamorphic rocks, monazites are likely to register younger deformation/metamorphic events, especially low-T events, whereas the older high-T events may be better preserved in zircon because it is resistant to younger low-T events.

4.1. Electron microprobe Th-U-Pb chemical dating in monazites

In situ Th-U-Pb chemical monazite dating of samples from the three domains mapped in the Daltongunj-Chipadohar area (Fig. 5a) constrain the ages of the four deformation events in western CGC. This data is compared to new monazite data from the Simultala-Chakai area in NE-CGC to understand if spatial variations exist in ages of the deformation-metamorphism and magmatic events in the three lithodemic units existing across distant sectors. The age data from NE-CGC (this study) is in addition to the age dataset of Sequeira et al. (2020) from overlapping areas; together, this makes the comparison between NE and western CGC more robust. A total of 16 samples from the Daltongunj-Chipadohar area and the Simultala-Chakai area (Fig. 2a) were analyzed, using a CAMECA SX-100 electron probe microanalyzer fitted with four wavelength dispersive spectrometers at the

Fig. 5. (a) Structural map of the Daltongunj-Chipadohar area. The WSW part of the area is poorly exposed. Lithologies simplified after the District Resource Maps of Palamu-Garhwa (Geological Survey of India, 2002) in 1:300,000 scale published by the Geological Survey of India. Sectors A and B correspond to (i) the D1-D2 steep-dipping (> 70°) Sector of basement rocks and (ii) the shallowly-dipping carapace (< 40°) respectively. Sector C (dip between 40 and 70°) is the zone of transition between sectors A and B where steeply-dipping rocks at structurally deeper levels are rotated in the overlying carapace. (b) Geological section along A–A'. The height (in meters) is adopted from the digital elevation data in the website (www.floodmap.net). (c–f) Southern hemisphere equal area stereographic plots of mesoscale structures, e.g. poles to foliation (back and green squares), fold axis lineation (blue dot) and stretching lineation (red dot). (c) In Sector A, D2 planar fabric in gneisses and granitoid, D2 fold axis in gneisses, and D2 stretching lineation in foliated granitoid. (d) In sector B, D3 planar fabric in gneiss and granitoid mylonite, D3 fold axis in gneiss and D3 stretching lineation in granitoid mylonite. (e) In the Northern shear zone and (f) in the southern shear zone, D4 planar fabric in gneiss and granitoids, D4 fold axes in gneiss and stretching lineation in granitoids.
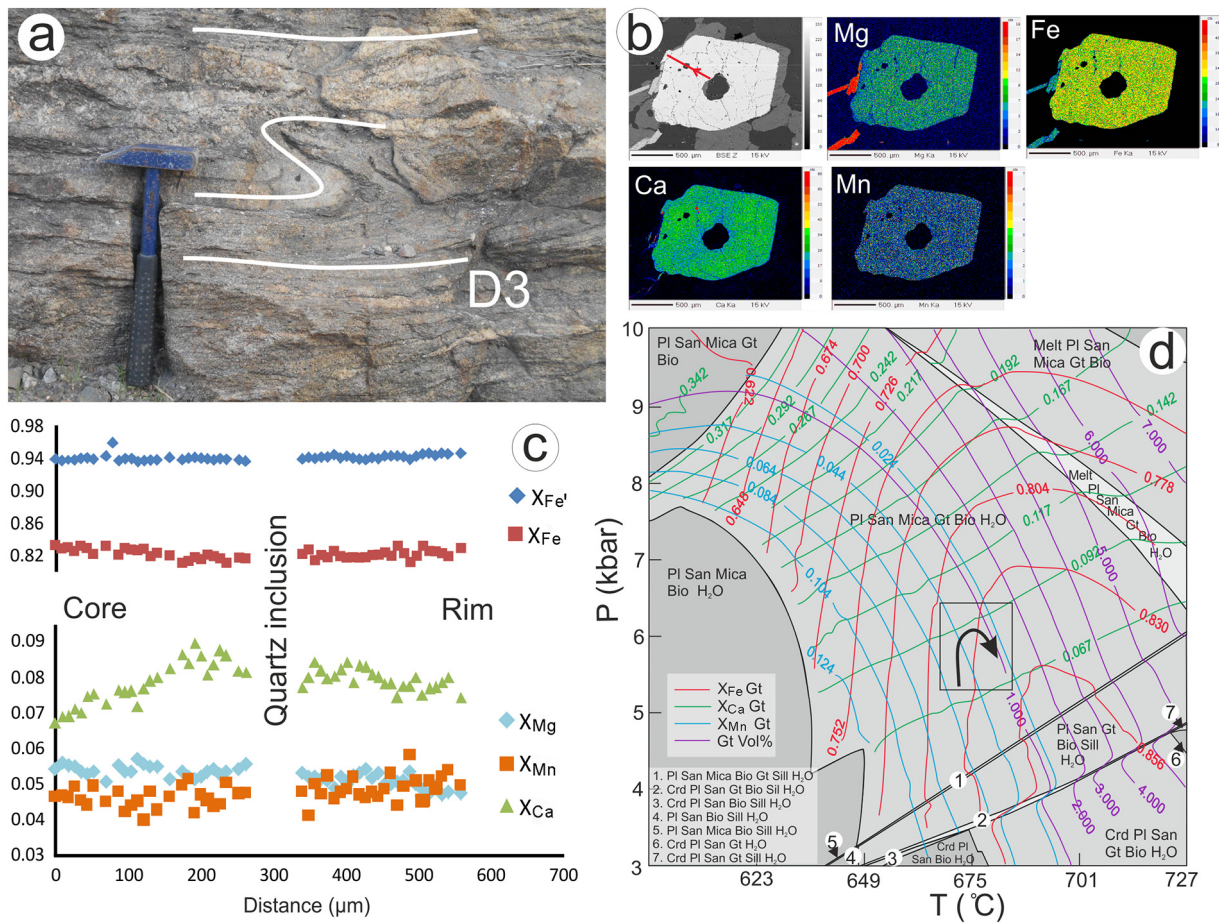
Fig. 6. Details of sample SM-21 used for P-T pseudosection analysis. (a) Outcrop scale photo of the mica schist sample showing flat-lying D3 foliation with pre-D3 intrafolial folds. (b) Back scatter electron image, and X-ray element maps for Fe, Mn, Mg and Ca of the analyzed garnet. The line used in garnet analysis is shown in red in the BSE image. (c) Variations in $X_{Fe'}$, X_{Fe}, X_{Mn}, X_{Mg} and X_{Ca} in the garnet is shown. (d) Results of MnNCKFMASH P-T pseudosection analysis. The major element oxide wt.% of the whole rock are: $SiO_2 = 81.18$; $Al_2O_3 = 9.30$; $TiO_2 = 0.34$; $FeO = 2.0$; $MnO = 0.01$; $MgO = 0.25$; $CaO = 0.37$; $Na_2O = 0.82$; $K_2O = 5.09$; $P_2O_5 = 0.05$; Loss on ignition = 0.55. The compositional isopleths and contours for garnet volume % are indicated. The reconstructed P-T path consistent with core to rim variations in garnet shown in black (details in text).

National Facility, Indian Institute of Technology, Kharagpur (see Appendix 1 for analytical procedure). The data, rock type and locations of the samples are provided in Supplementary material 3, and the textural context along with the Th and Y element X-ray maps of representative monazite grains are shown in Fig. 7. The age populations in Fig. 7 were processed using the Isoplot 4.15 software (Ludwig, 2012).

Four basement gneisses and three foliated granitoids from the Daltongunj-Chipadohar sector, and five basement gneisses, one foliated granitoid and three mica schists within the supracrustal unit in the Simultala-Chakai area were analyzed. In both areas, the anatectic basement gneisses (quartz – K-feldspar – plagioclase – biotite ± hornblende ± garnet) are mineralogically similar, as are the foliated granitoids (quartz – K-feldspar – plagioclase – biotite ± hornblende ± garnet). The mica schists from the Simultala-Chakai areas consist of muscovite – biotite – quartz – garnet – minor K-feldspar and plagioclase ± sillimanite. But sillimanite-K-feldspar intergrowths are lacking.

In the basement gneisses from both areas, the monazite grains are subhedral to anhedral, with long axis varying between 50 and 100 μm, and exhibit patchy and nebulously zoned interiors with patchy variations in Th and Y (Fig. 7a); by comparison U and Pb variations are insignificant. The monazite grains typically occur within biotite aggregates defining the D1-D2 fabrics in the gneisses (Fig. 7a), less commonly they are lodged within recrystallized grains of quartz and feldspars, and in rare instances smaller monazites are hosted within garnets. In steeply-dipping (D1-D2 composite fabric) gneisses unaffected by D3 recumbent folding and distal from the D4 shear zones, monazite dates

obtained from Th-richer interiors can be grouped into two dominant age clusters with mean population ages at 1627 ± 6 Ma and 1355 ± 9 Ma; a subsidiary peak is noted at 1487 ± 8 Ma. The Early Mesoproterozoic ages are inferred to correspond to the D1 deformation event while the 1.35–1.45 Ga ages correspond to the D2 deformation and synchronous magmatic emplacement event (Fig. 2c; see section 4.2). Monazites in the basement gneisses within the shallow-dipping D3 carapace and in the D4 shear zones develop distinct Early Neoproterozoic (976 ± 6 Ma) Y-rich rims (5–15 μm) that mantle nebulously zoned patchy Early/Mid Mesoproterozoic cores (Fig. 7a). In biotite-rich basement gneisses within the carapace, entire monazite gains are Early Neoproterozoic in age. In SM-30, the Early Neoproterozoic younger ages are obtained in ill-defined patches at the rims of the monazite grains. Sequeira et al. (2020) and Sequeira and Bhattacharya (2020, 2021) assigned the Early Neoproterozoic age to the D3-D4 deformations. Notably, in the Simultala-Chakai sector in NE-CGC, monazites in the biotite-garnet gneisses yield a mean population age at 1279 ± 9 Ma besides the Early Mesoproterozoic (~1600 Ma) and the Early Neoproterozoic (1000–900 Ma) monazite dates (Fig. 7a).

In the foliated granitoids in and neighboring the southern shear zone in the Daltongunj-Chipadohar area (Fig. 5a), monazite grains (up to 140 μm in length) are subhedral to euhedral and lodged within partly recrystallized quartz and feldspar. In the three granitoids, monazite grains display patchy zoning in Th and Y, but distinct Y-rich rims are sometimes present (Fig. 7b-I). However, all the monazite grains from
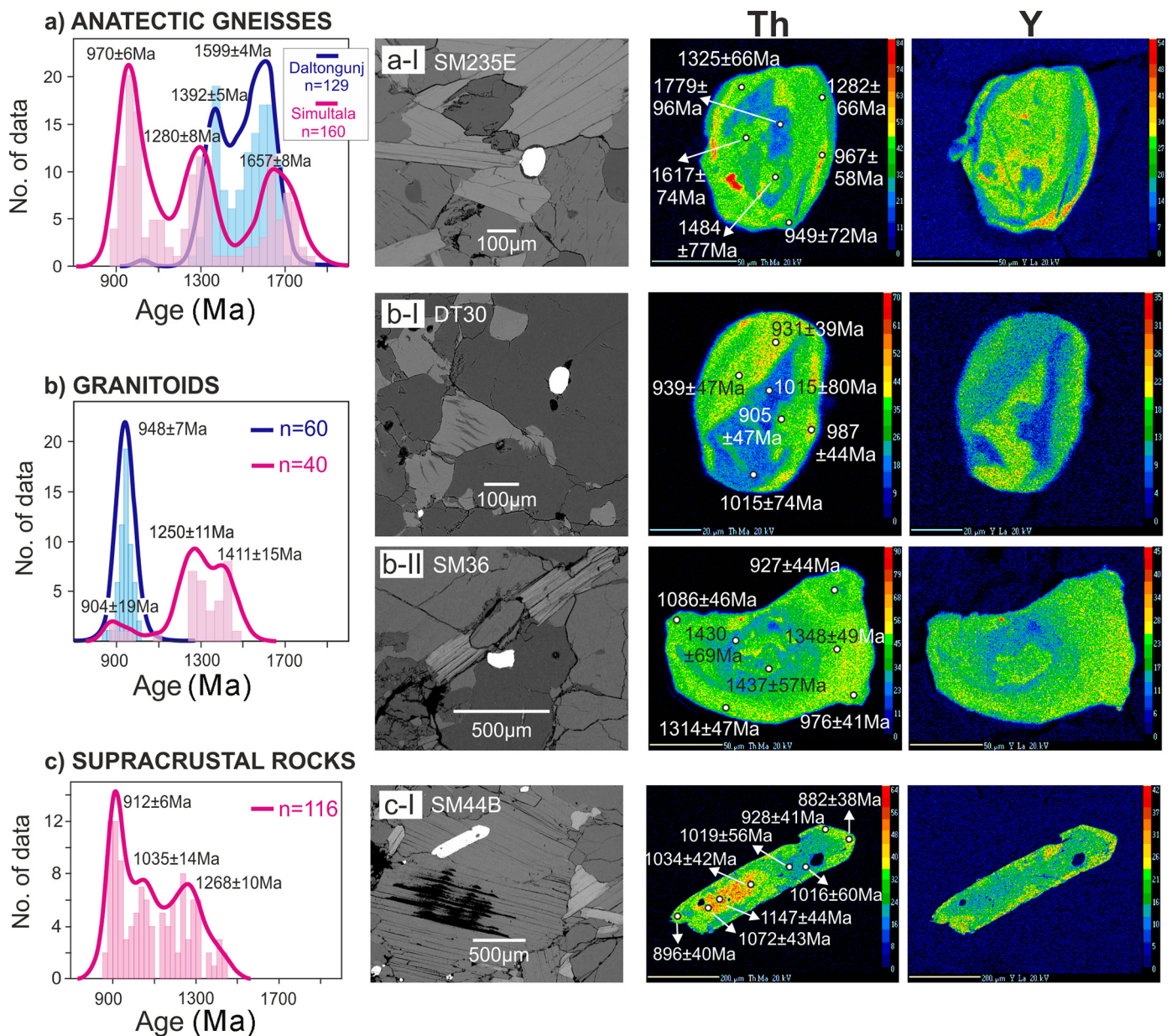
Fig. 7. Left panel compares summary probability-density plots of monazite dates in the Daltongunj-Chipadohar and the Simultala-Chakai areas in CGC for anatectic gneisses (a), granitoids (b) and supracrustal rocks (c). Peak ages with ±2σ errors are keyed to the figures. Number of spot ages is indicated. Back scatter electron (BSE) images of textural settings in monazites in representative samples are shown in the next column. X-ray element maps of Th and Y of the monazites in BSE images are shown in the next two columns. Spot dates with ±2σ errors are keyed to the Th maps.

the three samples yield only Early Neoproterozoic ages, with mean population ages at 932 ± 12 Ma, 946 ± 17 Ma and 948 ± 9 Ma (Fig. 7b-I). Since the monazite grains are locked within comparably rigid minerals (quartz and feldspars), we infer that the granitoids were emplaced in the Early Neoproterozoic.

The analyzed granitoid sample (SM-36) from Simultala possesses the steeply-dipping D2 fabric and is located distal from the D4 shear zones. The monazites in the sample have nebulously zoned Th-poor elliptical cores that sharply terminate against homogenous Th-rich mantles; rimwards the mantles grade into thin Th-poor rims (Fig. 7b-II). The three chemical domains are characterized by three age clusters with mean ages at 1411 ± 15 Ma, 1250 ± 11 Ma and 904 ± 19 Ma (Fig. 7b-II), with the oldest dates obtained in the cores comprising >50% of the analyzed spot ages. We infer that ~1400 Ma is the emplacement age for the granitoids (cf. U-Pb zircons ages reported by

Mukherjee et al., 2017, 2018a; this study, see section 4.2). This is a rare Mid-Mesoproterozoic granitoid that contained monazite. A granitoid sample (GM-75) located close to SM-36 is the only other Mid-Mesoproterozoic granitoid reported from the CGC with ~1.4 Ga chemical dates from monazites (Sequeira et al., 2020). Most other granitoids in the CGC that contain monazites are Early Neoproterozoic in age (Karmakar et al., 2011; Rekha et al., 2011; Mukherjee et al., 2018b; Sequeira and Bhattacharya, 2020, 2021; Sequeira et al., 2020).

The supracrustal rocks in the Daltongunj-Chipadohar sector are highly weathered, and monazite dating was difficult to perform. In the Simultala-Chakai area, the supracrustal rocks (SM-24C, SM-44B and SM-204XZ) in the shallow-dipping carapace possess the penetrative D3 foliation. SM-24C contains small monazites (long axis < 20 μm), whereas the other two samples contain larger monazites (40–80 μm). In SM-44B located within a D4 shear zone, some of the analyzed

monazites grains are as large as 250 μm (long axis) (Fig. 7c). All three samples yield Early Neoproterozoic ages with peak values at 962 ± 14 Ma, 934 ± 42 Ma and 907 ± 6 Ma. Among the three samples, SM-204XZ and SM-24C yield a second prominent age population around 1261 ± 15 Ma and 1264 ± 14 Ma respectively. A Mid-Mesoproterozoic age (1401 ± 18 Ma) from the grain interior is obtained in SM-204XZ, but this age is lacking in the other two samples. The significance of the ~1260 Ma peak in the three lithodemic units of NE CGC around Simultala is yet to be understood.

4.2. SIMS U-Pb (zircon) geochronology

A basement gneiss (DT-36), four foliated granitoids including KM-8A which is the northern most sample in the CGC ever dated, and an anatectic granitoid (GY-68; within the shallowly-dipping D3 carapace, Fig. 4a) at the northern margin of the CGC were selected for U-Pb zircon dating (locations in Fig. 2a). The samples were dated to constrain the age of (i) the D1 deformation in the CGC, (ii) the emplacement age of the post-D1 granitoids, and (iii) the age of accretion-induced *syn*-thrusting (D3) melting event in the CGC (Fig. 4a) at the northern margin of the CGC. Except for SM-8a, the three other dated granitoids possess the penetrative D2 steeply-dipping N-trending fabric (Fig. 4c), but lack the D1 fabric typical of the anatectic basement gneisses, and have not been affected by the D3-D4 deformations. No U-Pb zircon dates exist in the areas from which the rocks were sampled (Table 1). The zircons from the five samples were analyzed in two sessions using the secondary ion mass spectrometer (SIMS) at UCLA, California, USA. A brief description of the analytical procedure is given in the Appendix. Analytical data from the zircons (Fig. 8) is provided in Table 1. Th/U ratios of all analyzed spots in zircons in the basement gneiss and the four granitoids are shown in Fig. 9a; the U-Pb concordia plots (with probability density variations of Pb-Pb ages as insets) in the individual samples are depicted in Fig. 9b–f. Data points with upto 15% discordance are included for the granitoid samples in Table 1, but inferences are drawn only from points with <10% discordance (as suggested by Spencer et al., 2016) and plotted in Fig. 9c–f.

Th/U ratios are commonly used to distinguish metamorphic and magmatic zircons (Williams and Claesson, 1987; Rubatto, 2002; Linnemann et al., 2011; Kirkland et al., 2015). Kirkland et al. (2015) suggested that magmatic zircons are likely to have Th/U ratio > 0.5, while much lower values are suggested for metamorphic zircons Th/U < 0.1. Th/U values between 0.1 and 1.5 are suggested for zircons in magmatic rocks of felsic to intermediate composition (Hoskin and Schaltegger, 2003). However, the initial Th and U contents in the system, and the timing of monazite crystallization and its breakdown are known to influence the Th/U ratios in zircons (Yakymchuk et al., 2018). Yakymchuk et al. (2018) postulate that zircons with Th/U < 0.1 are metamorphic, but zircons with Th/U > 0.1 can be either igneous or metamorphic. None of the U-Pb dated ~1.45 Ga CGC granitoids in this study contain monazites, and almost all analyzed zircons (Table 1) have Th/U ratios >0.1 (as cf. Mukherjee et al., 2018a). Therefore, following Yakymchuk et al. (2018) we interpret the Pb-Pb zircon dates to correspond with the age of emplacement of the granitoids. However, Mukherjee et al. (2018b) report monazites in similar rocks in Dumka-Deoghar, but these monazites are Early Neoproterozoic and possibly grew during the D3-D4 deformations in the CGC.

4.2.1. The CGC basement gneiss

Sample No. DT-36 (24°00.53′N, 83°58.54′E): In the basement gneiss, the zircon grains (long axis: 80–120 μm) are euhedral to subhedral in shape, with common rationally developed faces (Fig. 8a). The weakly luminous zircons exhibit nebulous chemical zones in the grain interiors, but the fainter luminescent mantles are chemically uniform (Fig. 8a). The cores of the grains lack well-developed terminations and share diffuse interfaces with the mantles (Fig. 8a). Almost all the points analyzed in the sample show a small reverse discordance

(Table 1), with the youngest dates corresponding to maximum discordance. Analytical processes such as differential spluttering behavior between the sample zircons and the standard producing this reverse discordance (Wiedenbeck, 1995; Corfu, 2013) is ruled out since at least four points within the same age range in the sample show a normal discordance. Similarly, the matrix effect resulting from high U contents lead to reverse discordance in zircon (White and Ireland, 2012). However this does not hold true for this sample because the matrix effect is insignificant until the U concentrations in the zircon is in the high 1000s (ppm). Also there is no clear relationship between U content and reverse discordance in this dataset, as expected for the matrix effect. It is possible therefore that the zircon grains experienced a U-loss event through metamorphic fluid alteration or chemical weathering rather than a simple intracrystalline redistribution of radiogenic lead (Mattinson et al., 1996). However, the susceptibility of higher-U zircons to alteration due to radiation damage accumulation is not evident in the sample due to the lack of a clear relationship between U content and the overall discordance (+ or -) but it is a possibility that the originally higher-U grains witnessed U-loss, causing the U concentrations to approach the same range as in the other zircon zones.

Nonetheless, the dates are too closely spaced within the error limits to produce a meaningful discordia line in $^{207}Pb/^{235}U$ versus $^{206}Pb/^{238}U$ diagram (Fig. 9b). In a majority of the analyzed spots with older Pb-Pb dates (>1500 Ma) the Th/U > 0.3 while younger dates (1446–1495 Ma) have Th/U around 0.1–0.2 (barring 4 spots, Fig. 9a). In $^{207}Pb/^{206}Pb$ probability-density plots, the dates can be statistically resolved into three populations with mean age, e.g. 1588 ± 11 Ma, 1501 ± 13 Ma and 1453 ± 30 Ma (Fig. 9b). The older dates are obtained in the zoned grain interiors, while the youngest ages are obtained close to the grain margins; some of these youngest ages are also obtained in the core of chemically homogeneous grains that lack zoned interiors (Fig. 8a). We suggest the lower Th/U ratio and the increased reverse discordance for the younger ages to correspond to metamorphic zircon growth of individual crystals and overgrowths on older magmatic cores. The cores were possibly disturbed by the younger event, the age of which corresponds to the emplacement of a suite of A-type granitoids in the CGC (see later).

4.2.2. The Mid Mesoproterozoic granitoids

The D2 fabric in the granitoids is defined by the shape preferred aggregates biotite (± hornblende) in a dynamically recrystallized mosaic of quartz and modally equivalent amounts of K-feldspar and plagioclase, with apatite, ilmenite and zircon (rarely titanite) occurring as accessory phases. Sub-cm sized, sieve-textured garnet porphyroblasts occur sporadically (<5 vol% of rock) and is invariably wrapped around by the D2 biotite± hornblende aggregates.

GY-11 (24°35.56′N, 85°31.80′E), **GY-64** (24°13.49′N, 84°51.08′E): Zircon grains in GY-11 are well-faceted, large (long axis: 350–400 μm), and exhibit concentric oscillatory zoning, although some grains have poorly-luminescent rarely nebulous cores (Fig. 8b). In GY-64, the zircon grains have similar internal structures, but some grains are non-faceted and ellipsoidal in shape (Fig. 8c). The $^{207}Pb/^{235}U$ versus $^{206}Pb/^{238}U$ diagrams display the concordant to near-concordance of the zircon grains in both samples (Fig. 9c, d). In the probability density $^{207}Pb/^{206}Pb$ plots, zircons in GY-11 exhibit a prominent age population, 1448 ± 11 Ma and a small subsidiary peak at 1395 ± 15 Ma (Fig. 9c). Considering the closeness of the ages and their ±1σ error limits, the weighted mean age of 1428 ± 21 Ma for the sample is possibly more representative of the data. An identical weighted mean age of 1428 ± 22 Ma is calculated for GY-64 that also shows a bimodal population in the probability density plot (Fig. 9d). For data points with <10% discordance, the Th/U concentrations in the analyzed zircons from the two samples are >0.2, although the Th/U variation in GY-64 is considerably more than in GY-11 (Fig. 9a). Therefore, since the oscillatory zoning patterns in the zircon grains are continuous from core to rim (Fig. 8b, c), and the ages obtained from the cores and the rims overlap within the

Table 1
SIMS U–Pb isotope data and dates (±1σ errors) in zircon in the basement gneiss and granitoids in north and central CGC (sample locations in Fig. 2a).

Th (ppm)	U (ppm)	Th/U	Hf (ppm)	207Pb*/235U	1 s.e.	206Pb*/238U	1 s.e.	Correlation of concordia ellipses	Age (Ma) 207Pb/206Pb	1 s.e.	206Pb/238U	1 s.e.	207Pb/235U	1 s.e.	% Radiogenic 206Pb	% disc
DT-36																
42.24578	1138.639	0.037102	n/a	3.587	0.3641	0.2773	0.02787	0.9981	1504	11.96	1578	140.6	1547	80.59	99.85	−4.6895
923.9023	2027.383	0.455712	n/a	3.656	0.2372	0.2705	0.01732	0.9892	1587	17.74	1543	87.87	1562	51.72	99.71	2.8516
182.8204	2461.379	0.074276	n/a	3.721	0.3012	0.2745	0.02215	0.9969	1592	11.97	1564	112	1576	64.78	99.9	1.7903
183.7044	2672.178	0.068747	n/a	3.654	0.308	0.2696	0.0226	0.9956	1592	14.77	1539	114.7	1561	67.2	99.93	3.4438
536.1247	1179.075	0.454699	n/a	3.461	0.2694	0.2641	0.02039	0.9871	1529	23.44	1511	104	1518	61.31	99.29	1.1913
456.3785	925.8073	0.492952	n/a	3.934	0.2251	0.2881	0.01635	0.9891	1606	15.67	1632	81.83	1621	46.31	99.68	−1.59314
341.4672	805.0633	0.42415	n/a	3.949	0.1874	0.2966	0.0138	0.9848	1559	15.47	1674	68.61	1624	38.44	99.74	−6.86977
28.25783	1514.896	0.018653	n/a	4.031	0.5139	0.3077	0.03907	0.999	1528	10.96	1729	192.6	1640	103.7	99.83	−11.6252
245.0032	1477.138	0.165863	n/a	3.912	0.1944	0.3041	0.01453	0.9693	1494	23.13	1712	71.84	1616	40.19	99.24	−12.7336
1144.501	1940.584	0.589772	n/a	4.259	0.312	0.3195	0.02332	0.9964	1561	11.61	1787	113.9	1685	60.24	99.26	−12.6469
2957.333	895.2725	0.330328	n/a	4.266	0.193	0.3226	0.01426	0.9829	1546	15.67	1803	69.49	1687	37.22	99.68	−14.254
253.0739	382.8468	0.661032	n/a	4.436	0.2033	0.3286	0.01462	0.9708	1584	20.56	1832	70.96	1719	37.98	99.39	−13.5371
1037.469	1166.055	0.889725	n/a	4.706	0.2424	0.3426	0.01647	0.9662	1617	24.92	1899	79.06	1768	43.14	98.51	−14.8499
188.7966	547.9204	0.344569	n/a	4.543	0.2231	0.3289	0.01591	0.9854	1628	15.52	1833	77.16	1739	40.86	99.79	−11.1839
GY-11																
90.16056	143.4434	0.628544	9577.075	2.801	0.2141	0.2314	0.01873	0.9605	1378	43.38	1342	98.06	1356	57.19	99.64	2.682563
206.9028	364.5865	0.5675	11,471.97	2.875	0.1358	0.2291	0.01257	0.9632	1447	30.05	1330	65.92	1375	35.58	99.75	8.796992
89.39378	523.5305	0.170752	12,532.29	3.067	0.1817	0.2488	0.01375	0.9435	1413	37.58	1432	70.99	1425	45.36	99.68	−1.32682
172.206	340.9559	0.505068	11,868.73	2.757	0.1974	0.2218	0.01353	0.9565	1429	42.35	1291	71.4	1344	53.35	99.7	10.68939
154.2506	304.3848	0.506762	10,172.22	2.733	0.1377	0.2247	0.01144	0.9679	1387	24.63	1307	60.19	1337	37.45	99.67	6.120888
856.2378	1800.99	0.475426	13,968.85	2.944	0.1412	0.2336	0.01119	0.9823	1455	17.17	1353	58.47	1393	36.35	99.92	7.538803
113.9946	227.4727	0.501135	10,794.73	3.02	0.1613	0.2413	0.01091	0.9453	1442	34.71	1394	56.63	1413	40.75	99.69	3.443329
121.2152	245.0832	0.494588	11,164.13	2.931	0.1696	0.2308	0.01251	0.9675	1470	27.98	1339	65.54	1390	43.8	99.77	9.78342
421.2818	474.0188	0.888745	10,733.16	2.822	0.1424	0.2324	0.01101	0.9437	1384	32.07	1347	57.62	1361	37.83	99.76	2.746845
411.3136	2922.881	0.140722	12,402.31	2.81	0.2155	0.2311	0.01862	0.9918	1387	20.77	1340	97.51	1358	57.44	99.96	3.507463
186.0081	916.8114	0.202886	18,976.29	2.908	0.1401	0.2311	0.0101	0.9834	1452	18.01	1340	52.91	1384	36.4	99.82	8.358209
246.4559	436.3223	0.564848	11,567.74	2.783	0.1282	0.2248	0.01162	0.9343	1421	35.47	1307	61.15	1351	34.41	99.79	8.722265
610.357	910.3411	0.670471	11,807.17	2.765	0.1349	0.221	0.01157	0.9687	1442	25.05	1287	61.11	1346	36.39	99.66	12.04351
164.7938	315.6374	0.522098	12,162.89	2.887	0.145	0.2239	0.01075	0.9503	1498	29.59	1303	56.62	1378	37.88	99.9	14.96546
GY-64																
171.1198	145.0469	1.179754	12,203.93	2.71	0.1462	0.2244	0.01078	0.9397	1374	35.84	1305	56.77	1331	40	99.71	5.287356
87.15734	108.0256	0.806821	12,292.86	2.732	0.3246	0.2217	0.02275	0.9412	1412	78.8	1291	120	1337	88.32	99.13	9.372579
194.6343	131.2061	1.483424	11,164.13	2.77	0.1502	0.23	0.01179	0.9573	1368	30.21	1335	61.78	1347	40.46	99.85	2.47191
177.0623	132.894	1.332357	12,395.47	2.917	0.1887	0.2336	0.01286	0.8759	1438	59.59	1353	67.2	1386	48.91	99.81	6.282336
244.4751	724.1094	0.337622	14,550.31	2.895	0.1252	0.2317	0.009824	0.9939	1438	9.175	1344	51.41	1381	32.63	99.95	6.994048
350.2268	123.3574	2.839123	10,397.97	2.776	0.2074	0.2272	0.01331	0.9158	1395	60.61	1320	69.9	1349	55.79	99.41	5.681818
276.6798	85.63283	3.231002	10,322.72	2.743	0.1899	0.2307	0.01512	0.8092	1344	80.69	1338	79.21	1340	51.52	98.5	0.44843
1330.363	179.677	0.740419	12,805.92	2.925	0.1795	0.2337	0.01424	0.947	1442	37.94	1354	74.39	1388	46.44	99.71	6.499261
205.4971	1069.285	0.192182	15,213.87	2.433	0.1174	0.2048	0.01033	0.981	1342	19.04	1201	55.27	1252	34.71	99.84	11.74022
237.3823	147.0724	1.614051	11,328.31	2.753	0.1505	0.2209	0.009751	0.8687	1434	52.05	1287	51.48	1343	40.72	99.76	11.42191
37.87255	980.9516	0.038608	14,940.24	2.414	0.1123	0.2025	0.009003	0.9917	1348	11.98	1189	48.26	1247	33.39	99.79	13.37258
416.7106	109.4322	1.340653	11,232.54	2.874	0.2118	0.2248	0.01407	0.9563	1482	43.47	1307	74.04	1375	55.51	99.75	13.38944
KM-8a																
530.6118	992.2043	0.534781	13,052.19	2.747	0.1376	0.222	0.01016	0.9694	1420	24.08	1292	53.62	1341	37.28	99.83	9.907121
83.64293	174.0788	0.480489	12,286.02	2.664	0.1396	0.2176	0.01127	0.8524	1400	54.24	1269	59.66	1319	38.67	99.38	10.32309
1011.6623	184.7126	0.550381	11,444.6	2.584	0.181	0.2212	0.01481	0.8921	1309	62.03	1288	78.16	1296	51.29	98.74	1.630435
416.2977	829.3219	0.501974	12,457.04	2.802	0.1338	0.2275	0.009933	0.9776	1411	20.09	1321	52.17	1356	35.73	99.65	6.81302

1407.041	1423.182	0.986859	10,787.89	2.752	0.1212	0.2239	0.01008	0.996	1407	7.834	1302	53.11	1343	32.79	99.89	8.064516
115.7838	240.976	0.480479	11,923.46	2.856	0.1545	0.2305	0.01184	0.9531	1423	31.28	1337	62.02	1371	40.68	99.63	6.432311
413.1028	804.8473	0.513269	13,202.68	2.77	0.1156	0.2253	0.009578	0.9867	1408	13.24	1310	50.39	1348	31.14	99.76	7.480916
341.0893	559.2578	0.609896	11,848.21	2.837	0.1164	0.2275	0.008702	0.9695	1435	19.38	1321	45.7	1365	30.8	99.81	8.629826
1316.945	1479.164	0.890331	11,383.04	2.745	0.1391	0.2222	0.01057	0.9677	1417	24.6	1293	55.74	1341	37.71	99.84	9.590101
392.0802	878.5523	0.44628	10,787.89	2.334	0.1738	0.1996	0.01375	0.7711	1311	94.65	1173	73.89	1223	52.93	98.85	11.76471
132.653	251.019	0.528458	11,745.6	2.666	0.1563	0.2141	0.01274	0.9806	1432	22.26	1251	67.63	1319	43.31	99.6	14.46843
1214.707	1699.716	0.714653	10,917.87	2.654	0.118	0.2133	0.009539	0.9938	1431	9.454	1247	50.68	1316	32.78	99.8	14.75541
SM-8a																
309.5688	516.6107	0.59923	n/a	3.099	0.1793	0.2575	0.01399	0.9455	1367	36.28	1477	71.73	1432	44.41	99.21	−7.44753
480.3985	651.9246	0.736893	n/a	3.778	0.1921	0.2696	0.01232	0.9253	1654	35.81	1539	62.54	1588	40.82	98.93	7.472385
381.2442	865.0478	0.44072	n/a	3.203	0.3398	0.2597	0.02656	0.9676	1414	51.26	1488	135.9	1458	82.09	98.81	−4.97312
1334.163	4873.159	0.273778	n/a	3.469	0.3309	0.2802	0.02659	0.9933	1421	21.01	1592	133.9	1520	75.18	99.53	−10.7412
1200.996	1496.203	0.802696	n/a	3.121	0.2231	0.2552	0.01787	0.9793	1397	27.75	1465	91.77	1438	54.96	99.18	−4.64164
1153.725	1130.716	1.020349	n/a	3.191	0.2388	0.2605	0.01907	0.9796	1400	28.83	1493	97.5	1455	57.86	99.02	−6.22907
627.9769	988.1168	0.635529	n/a	3.075	0.2123	0.2546	0.01678	0.9722	1374	31.15	1462	86.2	1426	52.89	99.07	−6.01915
1564.946	3468.871	0.45114	n/a	3.35	0.228	0.2691	0.01822	0.9962	1432	11.32	1536	92.57	1493	53.23	99.67	−6.77083
3468.871	4202.015	0.467364	n/a	3.645	0.2227	0.29	0.01741	0.9961	1450	10.35	1641	87.02	1559	48.69	99.72	−11.6392
4202.015	792.9734	0.664705	n/a	3.325	0.1818	0.2744	0.01408	0.9572	1380	30.48	1563	71.21	1487	42.68	99.18	−11.7083
527.0932	792.9734	0.664705	n/a	3.325	0.1818	0.2744	0.01408	0.9572	1380	30.48	1563	71.21	1487	42.68	99.18	−11.7083
527.0932	197.1584	0.574553	n/a	3.196	0.1891	0.2699	0.01356	0.889	1336	52.59	1540	68.84	1456	45.76	98.34	−13.2468
113.278																
CY-68																
21.66154	1277.741	0.016953	14,440.86	1.307	0.0606	0.1383	0.006478	0.8764	885.4	47.9	835.1	36.68	849	26.67	99.42	6.023231
10.31319	934.253	0.011039	14,728.17	1.39	0.04758	0.1463	0.004831	0.9449	896.5	23.17	880	27.17	884.7	20.21	99.82	1.875
24.31971	1645.984	0.014775	14,557.15	1.263	0.05581	0.1329	0.005847	0.9871	897.1	14.61	804.2	33.27	829.3	25.04	99.87	11.55185
36.50512	1822.933	0.020025	15,200.19	1.3	0.05535	0.1328	0.005783	0.9844	898.2	15.93	803.9	32.91	829.3	24.83	99.92	11.73031
12.01289	965.4792	0.012442	15,576.43	1.349	0.07323	0.1363	0.007667	0.9891	903.5	17.14	823.9	43.49	845.7	32.33	99.88	9.661367
19.90433	2855.365	0.006971	16,082.65	1.279	0.05537	0.1414	0.005898	0.9768	904.1	18.41	852.5	33.31	867	23.94	99.88	6.052786
21.27176	1021.743	0.020819	15,213.87	1.293	0.05471	0.1337	0.005777	0.9551	910.1	26.53	809.1	32.85	836.5	24.37	99.42	12.48301
30.18558	1514.891	0.019926	14,871.83	1.278	0.05052	0.1346	0.005403	0.9729	917.8	19.09	814.3	30.7	842.6	22.37	99.9	12.7103
15.50174	1667.646	0.009296	15,815.86	1.322	0.06205	0.1331	0.006104	0.9938	918	12.1	805.7	34.73	836.2	27.65	99.94	13.93819
24.85006	1483.383	0.016752	14,461.38	1.312	0.05533	0.1375	0.005479	0.9175	921	34.34	830.5	31.05	855.6	24.19	98.78	10.89705
46.56272	2041.235	0.022811	14,878.67	1.385	0.06224	0.1362	0.006128	0.982	924.5	18.71	823.3	34.77	851.2	27.33	99.94	12.292
1.512474	430.9773	0.003509	16,855.65	1.316	0.075	0.1429	0.005667	0.8183	937.8	64.51	860.8	31.97	882.6	31.93	99.8	8.945167
27.95552	1669.615	0.016744	15,029.17	1.369	0.06794	0.1355	0.007192	0.9899	940.3	15.56	819.4	40.83	852.6	29.79	99.9	14.7547
17.68706	922.4377	0.019174	14,666.61	2.789	0.06369	0.1401	0.006218	0.9614	953.9	26.2	845	35.16	875.6	27.3	99.83	12.88757
991.0633	816.3813	1.213971	10,069.61	2.853	0.1514	0.2185	0.0114	0.9944	1479	11.45	1274	60.31	1353	40.59	99.81	16.09105
152.4614	334.4857	0.455809	13,100.07	2.837	0.1747	0.2229	0.01289	0.9636	1484	31.08	1297	67.96	1369	46.03	99.51	14.41789
1274.772	992.4856	1.284424	9809.661	2.806	0.1329	0.2216	0.009971	0.988	1485	13.94	1290	52.62	1365	35.17	99.85	15.11628
138.7872	289.475	0.479445	13,476.31	2.959	0.1424	0.2186	0.009724	0.9572	1489	28.88	1275	51.44	1357	38.01	99.83	16.78431
149.586	223.9563	0.667925	12,306.54	2.964	0.1654	0.23	0.0114	0.9126	1493	43.36	1335	59.76	1397	42.44	99.66	11.83521
173.0367	155.7651	1.110882	10,541.62	2.919	0.1461	0.2299	0.0116	0.9149	1499	38.97	1334	60.81	1398	37.42	99.6	12.36882
366.0097	381.1842	0.960191	11,417.24	3.005	0.1355	0.2248	0.009499	0.9671	1511	22.85	1307	50	1387	35.12	99.76	15.60826
336.4248	405.9401	0.828755	11,554.06	2.828	0.1293	0.2303	0.009649	0.955	1521	24.11	1336	50.56	1409	32.78	99.79	13.84731
141.5987	219.0332	0.646471	12,758.03	1.305	0.1465	0.2265	0.009983	0.9293	1437	37.32	1316	52.47	1363	38.87	99.8	9.194529
51.75127	2252.785	0.022972	14,981.28	1.31	0.05606	0.1349	0.005902	0.9862	933.4	14.87	815.9	33.52	848.1	24.69	99.95	14.40127
51.31676	1914.079	0.02681	15,083.89	1.265	0.05985	0.1354	0.006106	0.9808	934.2	18.26	818.4	34.67	850.2	26.3	99.87	14.14956
42.21124	1947.837	0.021671	15,042.85		0.05766	0.1321	0.005954	0.9772	913	19.96	799.7	33.9	830.2	25.85	99.93	14.16781
139.6818	290.8815	0.480202	14,263	2.784	0.1705	0.2222	0.01231	0.9652	1444	31.3	1293	64.93	1351	45.75	99.6	11.67827

error limits, we suggest that the weighted mean ages for the two samples (~1.43 Ga) correspond to the emplacement age of these granitoids.

Sample KM-8a (25°04.00′N, 86°31.47′E): In the sample, zircon grains are 200–400 μm long, euhedral and prismatic in shape with well-defined pyramidal terminations (Fig. 8d). The grains commonly consist of a weakly-luminescent core mantled by concentric rims of oscillatory zones. Some of the grains are poorly luminescent but still show faint oscillatory zoning from the core to the rim (Grain 4, Fig. 8d). The Th/U of the all the analyzed zircons are typically >0.4 (Fig. 9a). The analyzed spots are near-concordant in $^{207}Pb/^{235}U$ versus $^{206}Pb/^{238}U$ diagram (Fig. 9e); the $^{207}Pb/^{206}Pb$ dates yield a single population, with a weighted mean Pb-Pb age of 1411 ± 11 Ma (Fig. 9e); we interpret the date to be the emplacement age of the granitoid.

Sample No. SM-8a (24°43.22′N, 86°31.21′E): The rock is a granite protomylonite at the Tilauna village near Simultala (Fig. 2a). In the exposure, massive granites with weakly-recrystallized, euhedral and randomly oriented K-feldspar porphyries can be continuously traced from protomylonite to ultramylonite varieties. The steeply-dipping mylonite foliation strikes ENE (D4 fabric) and the stretching lineations plunge gently towards WSW. In horizontal sections (close to the X-Z section of the strain ellipsoid) the sense of shear is sinistral. The minerals in order of decreasing abundance are quartz, K-feldspar, plagioclase, biotite and minor hornblende. The zircon grains in this protomylonite granite are 80–130 μm long, and commonly euhedral with well-developed prismatic faces and well-developed terminations (Fig. 8e). The poorly luminous cores are either chemically homogenous, having faint oscillatory zones or nebulously zoned. The more luminous mantles around the cores show well-developed oscillatory concentric zoning (Fig. 8e).

The Th/U ratios of the analyzed spots lie between 0.1 and 1.0 (Fig. 9a). In $^{207}Pb/^{235}U$ versus $^{206}Pb/^{238}U$ plots (Fig. 9f) the spot dates are concordant to near concordant, but predominantly lie above the Stacey-Kramer's curve. The slight reverse discordance is possibly an inherent feature of the zircons. In $^{207}Pb/^{206}Pb$ probability-density plots, the majority of the data makes up the younger population with a mean age of 1417 ± 8 Ma (inset, Fig. 9f); a single date 1654 ± 72 Ma is obtained from the faintly luminescent chemically homogenous core with an embayed margin against the concentrically zoned mantle (Fig. 8e, grain 2). The older Mesoproterozoic ages were obtained in the nebulously zoned grain interiors, while the younger dates are obtained in the mantles as well as in grain interiors. The oldest date is tentatively interpreted to represent the age of zircon xenocrysts entrained from the protolith, possibly the anatectic gneisses (Acharyya, 2003; Rekha et al., 2011; Mukherjee et al., 2019). The weighted mean Pb-Pb age of 1417 ± 16 Ma from the other data points is interpreted to correspond with the magmatic age of the granitoid, similar to those in the samples discussed above.

In summary, the age of emplacement of the granitoids (1.40–1.45 Ga) overlaps with the ~1.45 Ga A-type granitoids reported by Mukherjee et al. (2017, 2018a, 2019) in a small area, Dumka-Deoghar (Supplementary Figure 1). But this study importantly demonstrates that the Mid Mesoproterozoic granitoids are expansive within CGC and extend across ~300 km (distance between Dumka and Gaya; Fig. 2a) effectively covering an area of at least 24,000 km² in the north and central parts of the CGC. The >1.5 Ga cores suggests that the 1.40–1.45 Ga granitoids were derived from the partial melting of the Early Mesoproterozoic (1.65–1.50) felsic basement gneisses, and experienced post emplacement modifications that continued till ~1.35 Ga.

4.2.3. Age of accretion at the northern margin of the CGC

The sample GY-68 (24°16.18′N, 84°49.48′E; location in Fig. 2a) is a granite mylonite in the shallowly-dipping D3 carapace at the northern margin of the CGC; the rock lacks both the D1 and D2 fabrics. Syn-D3 garnet-bearing leucosomes forming in situ layers are coalescent into diatexite pods (Fig. 4a) that formed at 9.5–11 kbar, 710 ± 10 °C (Sequeira and Bhattacharya, 2021). The penetrative D3 fabric in the

rock is defined by alternate dark and light colored mineral segregation layering. The melanocratic layers are defined by shape aggregates of biotite, rarely hornblende, and sphene is an accessory phase. Opaque mineral (<1 vol% of rock) is ilmenite. Garnet porphyroblasts are sieve-textured due to inclusions of biotite, quartz and feldspars, and occur exclusively in the quartz-feldspar bearing (± biotite) leucocratic layers. The larger garnet porphyroblasts are cm-sized. Both quartz and the feldspars are dynamically recrystallized; the mono-mineralic K-feldspar grains occur in lens-shaped aggregates and possibly were augen of former magmatic grains.

The zircon grains are large (long axes: 350–400 μm) and euhedral (Fig. 8f, g). Based on their internal structure, the zircon grains are classified into two textural types (Fig. 8f, g). Type-I grains (Fig. 8f) comprise nebulous to oscillatory zoned luminescent cores that are mantled by chemically homogenous to patchily zoned poorly luminescent rims. The cores share curved boundaries with the mantles, and the oscillatory zones in the cores terminate abruptly against the mantle. The evidence taken together indicates the older cores were dissolved during melting. Type-II zircon grains (Fig. 8g) are euhedral to subhedral in shape, similar in size to Type-I zircons, but relics of the embayed oscillatory zoned cores as in Type-I zircons are small, and in most cases lacking (Fig. 8f). Thin (< 5 μm) luminescent outermost rims (Fig. 8f) could not be analyzed.

Th/U in zoned cores in Type-I zircons are typically >0.4, whereas Type-II zircon grains and mantles in Type-I zircons are <0.1 (Fig. 9g). The cores of Type-I zircons are interpreted to be of magmatic origin in contrast to the poorly-luminescent metamorphic zircon mantles and Type-II grains. The magmatic zircons show a slight normal discordance as compared to the more concordant metamorphic zircons in $^{207}Pb/^{235}U$ versus $^{206}Pb/^{238}U$ diagram (Fig. 9h). The $^{207}Pb/^{206}Pb$ dates constitute two peaks, e.g. 1487 ± 13 Ma for the magmatic cores, and 922 ± 8 Ma for metamorphic zircons (Fig. 9h). The lack of a discordia between the two ages is because the anatexis occurred at a temperature (710 ± 10 °C) significantly lower than the closure temperature (900 °C; Cherniak and Watson, 2001) for U-Pb intra-crystalline diffusion. Therefore, the accretion of CGC with the northern domain is interpreted to have occurred in the Early Neoproterozoic; this is in consonance with the suggestion by Sequeira and Bhattacharya (2021) based on the analysis of monazite age data.

5. Geochemistry

The results of U-Pb zircon dating demonstrates that the post-D1, pre-D2 granitoids were emplaced around 1.45–1.4 Ga. Nine of these post-D1 pre-D2 foliated granitoids from Simultala and Daltongunj (a distance of ~360 km) covering an area > 35,000 km² (locations in Supplementary Figure 1) were selected for geochemical analyses. Most of these granitoids are sampled from the same Mid-Mesoproterozoic granitoid plutons dated in this study or by Sequeira et al. (2020). The granitoids were analyzed for major and trace elements (Table 2; analytical procedure in Appendix 1). Data in these samples are combined with those of Mukherjee et al. (2018a) from the Deogarh-Dumka area in E-CGC (locations in Supplementary Figure 1). The combined data are compared with the voluminous data set on the 1.5–1.3 Ga (mean ~ 1.40 Ga) A-type ferroan granitoids from North America compiled by du Bray et al. (2018); the authors suggest the granitoids with bimodal age populations, 1.46–1.41 Ga and 1.41–1.32 Ga, do not exhibit systematic variations in space. The SiO₂ contents of the 1.5–1.4 Ga CGC granitoids vary between 56 and 79 wt. %, are calc-alkaline to alkali-calcic in composition (Frost et al., 2001; Fig. 10a), and straddle the boundary between high-K and shoshonitic fields (Ewart, 1982; Le Maitre, 1989; Fig. 10b). Eight of the nine granitoids plot in the weakly peraluminous field. In [Fe₂O₃ᵀ/(Fe₂O₃ᵀ + MgO)] versus SiO₂ diagram, the felsic intrusives plot in the field of ferroan granitoids (Fig. 10c). With increasing silica, CaO, FeO, MgO, TiO₂, Al₂O₃
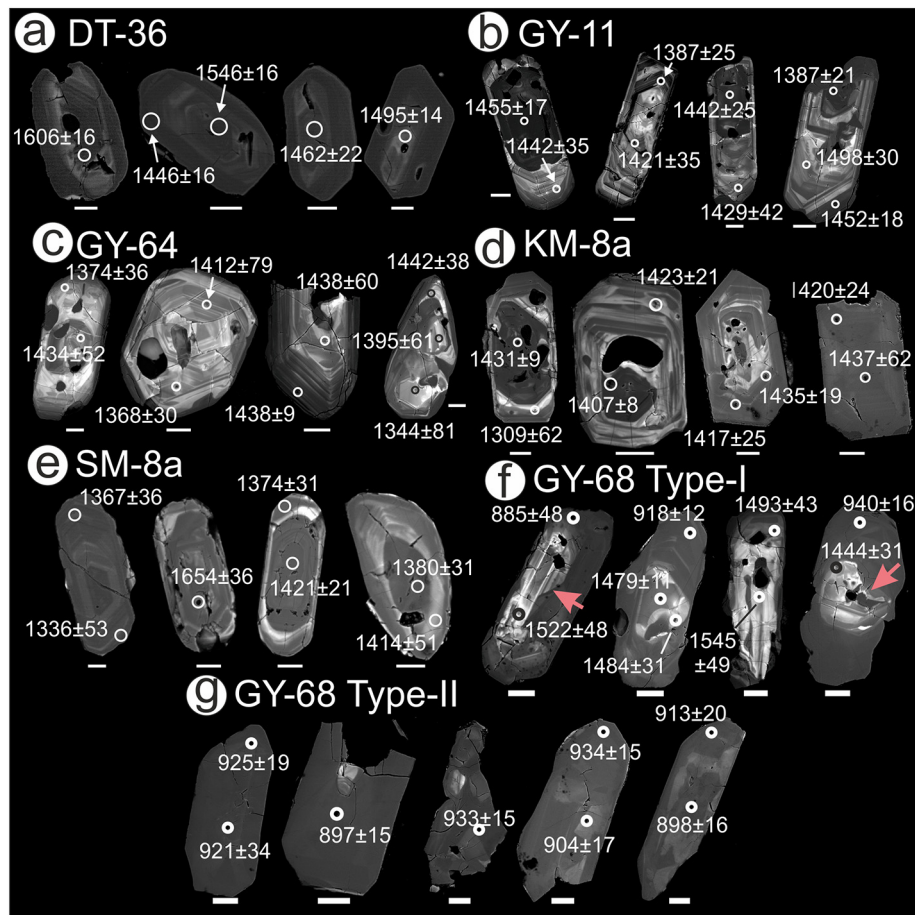
Fig. 8. Cathodoluminescence (CL) images of representative zircon grains in the (a) basement gneiss, (b–e) Mid-Mesoproterozoic A-type ferroan granitoids and in the (f, g) anatectic granitoid GY68 sample. 50 μm scale bars are shown for each grain. SIMS Pb-Pb dates with ±1σ errors are shown.

and P_2O_5 decrease, but K_2O and Na_2O abundances remain largely unchanged.

The trace element abundances (Nb, Ta, Sr, P, Ti and P) in the CGC granitoids (barring Pb which was not analyzed) are identical to those in the ~1.4 Ga North American granitoids. Nb/Ta values are >5 (Table 2) typical for peraluminous granites unmodified by hydrothermal activity (Ballouard et al., 2016), and correlate negatively with Ta possibly due to mica fractionation (Stepanov et al., 2014; Ballouard et al., 2016) (Fig. 10d). In Nb/Ta versus Zr/Hf diagrams, the granitoids plot in the field for peraluminous "barren" granites (Ballouard et al., 2016; Fig. 10e). Rb and Y + Nb concentrations straddle the boundary between the fields for *syn*-collisional and within-plate tectonic setting (Fig. 10f). In FeO^T/MgO vs. Zr + Nb + Ce + Y plots (Fig. 10g) after Whalen et al. (1987) most of the granitoids fall in the field of A-type granitoids. Most of the granites are weakly peraluminous to weakly metaluminous (Fig. 10h) in Shand's (1951) classification index.

Some of the Mid-Mesoproterozoic CGC granitoid samples show somewhat higher HREE abundances (Fig. 11a), compared to the ~1.4 Ga North American granitoids. The Eu/Eu* (Fig. 11b) values are lower, as are the Ba abundances (Fig. 11a). In the chondrite-normalized (Anders and Ebihara, 1982) REE plots (Fig. 11b), the granitoids have moderately negative slopes, but the magnitudes of the negative Eu anomalies are highly variable. The Eu/Eu* values, calculated using the formulations of Worrall and Pearson (2001), i.e. $Eu/Eu^* = Eu_N/\sqrt{[Sm_N \times Gd_N]}$, correlate negatively with the CaO + Na_2O contents in the rocks and $(La/Yb)_N$, i.e. larger Eu anomalies occur in granitoids with lower $(La/Yb)_N$ and CaO + Na_2O contents (Fig. 11c). The CaO + Na_2O contents is correlated with higher modal amounts of plagioclase, since among Ca, Na bearing phases

hornblende is a minor phase in the rock and apatite occurs in low modal amounts.

6. Discussion

Synthesis of the results of this study and existing studies form different parts of the CGC (Bhattacharya et al., 2019; Sequeira and Bhattacharya, 2020, 2021; Sequeira et al., 2020; this study) demonstrate similar lithologies, mesoscale structures, and chronology of magmato-metamorphic events across the CGC (Fig. 2). The most notable structural features are (a) the N/NNW trend of the Mid Mesoproterozoic D2 fabric (this study) in the basement rocks, except when modified in and neighboring the Early Neoproterozoic D3-D4 structures, and (b) the vast expanse of the shallow-dipping D3 carapace, especially well-exposed at higher structural levels, and the regional scale basement-piercing E-striking D4 transpressional shears (Fig. 2a, b). P-T pseudosection analyses indicates that the supracrustal rocks experienced D3 loading and D4 unloading at mid-crustal depths in a narrow temperature range between 665 and 690 °C.

The data suggests that the CGC sandwiched between the NIB and SIB (Figs. 1 and 2a) at the eastern end of the GIPFOB (Fig. 1) is a coherently-evolved Early Mesoproterozoic to Early Neoproterozoic crustal block. The northward translation (D3) of supracrustal rocks and nucleation of the steep D4 transpressional shear zones that aided oblique extrusion (Bhattacharya et al., 2019; Sequeira and Bhattacharya, 2020, 2021; Sequeira et al., 2020) accommodated the Grenvillian-age accretion-related shortening. The D3-D4 structures post-dated the emplacement of voluminous Grenvillian-age granitoids (Sequeira and Bhattacharya,
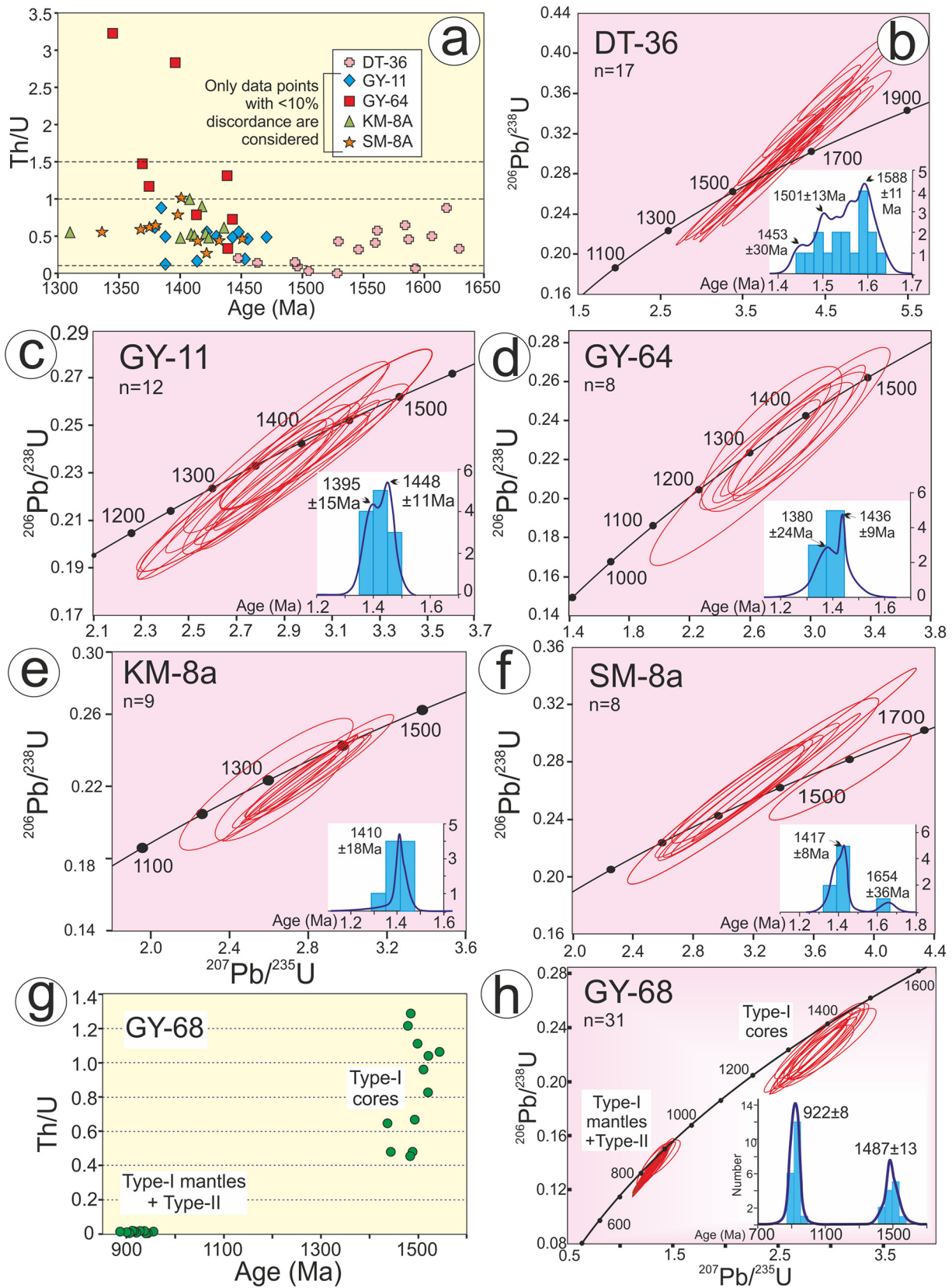
Fig. 9. (a) Th/U versus Pb-Pb dates of analyzed spots in zircon in the basement gneiss and the four Mid Mesoproterozoic granitoids. Broken lines from bottom upwards separate metamorphic zircons from zircons in felsic melts, transitional melts and mafic melts. (b–f) Concordia plots of spots dates in zircon grains in the basement gneiss (b) and the four Mid Mesoproterozoic granitoids (c–f). Error ellipses are ±2σ. (g) Th/U versus Pb-Pb dates in Type-I and Type-II zircon grains in sample GY-68 (see text for discussion). (h) Concordia plots of spots in zircon grains (error ellipses are ±2σ) in sample GY-68. Inset in (b–f, h) shows the probability density variations in Pb-Pb dates; mean population dates (±2σ errors) are indicated.

2020; Sequeira et al., 2020) intrusive into a basement comprising Mid Mesoproterozoic granitoids intrusive into Early Mesoproterozoic gneisses.

6.1. Variation in dates across the CGC

The monazite dates from the Daltongunj and Simultala sectors in western and eastern CGC (Fig. 7) demonstrate that although the deformation age ranges are broadly similar across the CGC, spatial variations in the dominance of age ranges exist across the CGC. To chronologically map the CGC (Fig. 12), the metamorphic and magmatic spot ages in monazites from the present (Supplementary material 3) are combined with published chemical dates in monazites from Ramgarh-Ormanjhi, central CGC (Sequeira and Bhattacharya, 2020), Gaya-Chatra, north-CGC (Sequeira and Bhattacharya, 2021), Bihar Mica Belt (Hazarika et al., 2017), Deogarh-Giridih-Dumka, east CGC (Mukherjee et al., 2018b; Sequeira et al., 2020), Rourkela area (Bhattacharya et al., 2016, 2019; Chowdhury and Lentz, 2011; Chakraborty et al., 2019), Kolomda-Ranchi area (Rekha et al., 2011), Purulia area (Karmakar et al., 2011) and Balarampur area (Chatterjee et al., 2010) along southern CGC (Fig. 12a). The monazite chemical dates have been segregated based on location (Fig. 12a - left panel) and based on lithology (Fig. 12a - right panel). These data are compared with available detrital and non-detrital Pb-Pb (zircon) dates from the Dumka-Deoghar area (Chatterjee et al., 2008; Rekha et al., 2011; Dey et al., 2017, 2019; Mukherjee et al., 2017, 2018a, 2019), Simultala-Gaya-Daltongunj area (this study) and the Rourkela area (Chakraborty et al., 2019) (Fig. 12b) to test the robustness of the monazite dates. The available Pb-Pb dates in non-detrital zircons are from anatectic gneisses and granitoids (Pb-Pb zircon dates are lacking in the supracrustal rocks) (Fig. 12b). The non-detrital Pb-Pb dates comprise three populations, e.g. 1.0–0.9 Ga, 1.5–1.4 Ga and 1.7–1.6 Ga. The Early Neoproterozoic and the Early Mesoproterozoic Pb-Pb dates are well corroborated by the monazites, but the ~1300 Ma monazite dates are younger than the ~1.45 Ga non-detrital zircon Pb-Pb dates. A small fraction of the older monazite chemical dates (1.45–1.40 Ga) coincides with non-detrital Pb-Pb dates. The three populations of monazite dates are prominent in north-CGC; the two older populations are subdued in the central parts, and are lacking in and neighboring the southern accretion zone which is dominantly Early Neoproterozoic (Fig. 12a - left panel). Lithologically the Early Neoproterozoic dates are prominent in all lithodemic units, the Mid Mesoproterozoic dates are present in granitoids and the supracrustal rocks, and the Early Mesoproterozoic dates are obtained in the anatectic gneisses (Fig. 12a - right panel).

6.2. Petrogenesis and emplacement temperature of the A type granitoids

A-type granites originate by different processes (Frost and Frost, 2011), e.g. by high degree of differentiation of tholeiitic and alkali basalts (Turner et al., 1992), partial melting of crustal protoliths (Clemens et al., 1986; Creaser et al., 1991; Frost and Frost, 1997; Huang et al., 2011), and assimilation of crustal rocks and/or mingling of crustally-derived melts with fractionating mafic magmas (Kemp et al., 2005; Zhang et al., 2012). In the CGC, the Mid-Mesoproterozoic A-type granitoids do not contain mesoscopic and/or microgranular mafic enclaves, and are not associated with contemporaneous mafic dykes and plutons. The lack of contemporaneous mafic emplacements and the absence of mafic enclaves preclude the involvement of voluminous mafic magmas in the formation of the 1.5–1.4 Ga granitoids (du Bray et al., 2018).

In a recent review of alkali-calcic and calc-alkalic ferroan metaluminous to peraluminous granitoids, Dall'Agnol et al. (2012) suggested that calc-alkalic varieties have SiO₂ contents >70 wt.% in contrast to alkali-calcic varieties that exhibit wide variations in SiO₂ contents. The prevalence of intermediate members in the alkali-calcic suite is attributed to incomplete mixing between mafic and felsic magmas

(Cullers et al., 1992; Frost et al., 1999) and/or assimilation of diverse crustal materials that caused the ascending peraluminous granitoids to evolve into metaluminous varieties (Anderson et al., 2003). By contrast, Dall'Agnol et al. (2012) suggested the calc-alkalic ferroan granitoids with Al₂O₃ contents <14 wt.% are formed by the partial melting of quartzofeldspathic precursors (Collins et al., 1982; King et al., 2001; Dall'Agnol and Oliveira, 2007; Oliveira et al., 2009); and this leads to absence of the intermediate members in these granitoids. Rudnick and Fountain (1995) propose that melts derived from upper crustal sources are likely to be characterized by Th > 10 ppm and Eu/Eu* ratios (<1); the corresponding values for middle and lower crustal sources are <6 ppm (Th), <15 ppm (Pb) and > 1 (Eu/Eu*). Th values (13–47 ppm) and Eu/Eu* values (0.1–0.8) suggest an upper crustal source for the 1.5–1.4 Ga CGC granitoids.

The A-type CGC granitoids with SiO₂ contents between 64 and 78 wt.% (only 2 samples have SiO₂ contents <70 wt.%) and Al₂O₃ contents <14 wt.% (most samples are in the range 12.1–12.9 wt.%) (Table 2) straddle the boundary between the alkali-calcic and calc-alkalic granitoids (Fig. 10a). The granitoids are interpreted to have been derived by partial melting of the basement felsic gneisses, dominated by garnet-biotite quartzofeldspathic gneisses, orthopyroxene – clinopyroxene – garnet ± hornblende bearing charnockite-enderbite gneisses, and garnet-sillimanite-biotite gneisses in order of decreasing abundance. The lack of sillimanite and pyroxenes (cf. Vielzeuf and Holloway, 1988; Pattino-Douce and Johnston, 2001) in the granitoids suggest that metapelite and charnockite-enderbite protolith did not contribute substantially to granitoid formation either because the rocks were too refractory to produce large amounts of melt or these rocks were volumetrically subordinate progenitors. The occurrence of local D2 diatexite at boundin necks (Sequeira et al., 2020) suggest that the melt productivity of the basement gneisses decreased substantially during D2. By default, garnet-biotite quartzofeldspathic gneisses appear to be the likely source rocks for the granitoids.

Skjerlie and Johnston (1993) suggested that ferroan peraluminous calc-alkaline melts are produced by low-degrees of fluid-absent melting at P > 6 kbar of biotite-bearing granodiorite at high-T (>900 °C). The local occurrence of garnets in the granitoids is difficult to assess; these garnets could qualify as a liquidus phase or as an incongruent phase produced on melting, or entrained from the protolith. Entrainment from progenitors could lead to somewhat higher HREE contents in these granitoids (Fig. 11a). The Eu/Eu* variations with (La/Yb)$_N$ and CaO + Na₂O in the granitoids (Fig. 11c) are instructive. These variations are best explained if plagioclase was a residual phase during dehydration melting that produced melts with pronounced negative Eu anomaly and relatively flatter REE spectra, e.g. (La/Yb)$_N$ ratio close to 1; the entrainment of the residual plagioclase during magma ascent would modify the magma compositions to higher (La/Yb)$_N$ and lower Eu/Eu* ratios for magmas with higher amounts of entrained plagioclase (CaO + Na₂O).

The emplacement temperatures of the A-type granitoids were estimated for the 9 samples (Table 2) from the zircon saturation temperature (T$_{Zr}$) using the formulations of Watson and Harrison (1983) and Boehnke et al. (2013). The T$_{Zr}$ values vary between 728 and 894 °C using the model of Watson and Harrison (1983); these values are 30–40 °C lower if the formulation of Boehnke et al. (2013) is adopted. The average T$_{Zr}$ value of 823 °C predicted by the equation of Watson and Harrison (1983) is marginally lower than the ~830 °C cutoff for A-type granitoids (Clemens and Vielzeuf, 1987; King et al., 2001) which are generally considered to be high temperature magmas. However, as the majority of the zircons in the samples analyzed (Fig. 8) do not contain xenocrysts and have very tightly clustered ages (Fig. 9), the T$_{Zr}$ values calculated for these inheritance-poor CGC granitoids should be a minimum estimate of the magma temperatures at the source (Miller et al., 2003) with the actual zircon saturation temperature up to 100 °C above the calculated T$_{Zr}$ values (Harrison et al., 2007). Using the equation of Watson and Harrison (1983), Mukherjee et al. (2018a)

Table 2

Bulk rock major element oxides (in wt.%) and trace elements (in ppm) in nine granitoid samples from the north and central parts of the CGC. Chondrite-normalized values of $(La/Yb)_N$ are after Anders and Ebihara (1982), Eu/Eu* computed from the equation of Worrall and Pearson (2001) and zircon saturation temperatures (T_{Zr}) calculated (in °C) using the formulations of Watson and Harrison (1983) and Boehnke et al. (2013) are included. Lat/Long of the samples is indicated.

	GM-76	GM-75	GY-12	DT-212	DT-269	KM-5	KM-6	SM-36	SM-35
Latitude (°N)	24°49.860	24°49.298'	24°34.96'	23°43.06'	24°06.393	25°13.856	25°13.851	24°40.043	24°40.698
Longitude (°E)	86°40.078	86°40.631'	85°34.03'	83°48.97'	83°49.270	86°33.940	86°33.765	86°10.209	86°10.59'
Major oxide data									
SiO_2	68.10	77.80	71.41	72.56	74.74	76.18	75.85	76.04	71.38
TiO_2	0.46	0.06	0.37	0.44	0.16	0.20	0.20	0.12	0.48
Al_2O_3	14.64	12.32	13.14	12.99	13.16	12.14	12.13	12.80	13.92
FeO^T	3.63	1.47	3.64	2.84	1.10	1.89	2.04	1.32	3.46
MnO	0.09	0.03	0.08	0.05	0.01	0.02	0.00	0.03	0.05
MgO	0.73	0.05	0.15	0.59	0.16	0.62	0.30	0.11	0.56
CaO	2.19	0.51	1.49	1.52	1.33	0.43	0.32	0.85	1.56
Na_2O	2.84	2.44	2.66	3.37	2.33	3.36	3.43	2.81	2.26
K_2O	4.82	6.20	6.01	3.49	6.04	4.99	5.24	5.05	6.33
P_2O_5	0.18	0.07	0.09	0.10	0.04	0.07	0.02	0.06	0.17
LOI	1.70	0.39	0.68	1.31	0.95	0.66	0.40	1.60	1.05
Total	99.36	101.35	99.72	99.26	100.01	100.58	99.92	100.77	101.21
Trace element data									
Ba	744	48	703	778	847	73	43	204	878
Be	1	2	3	5	2	4	7	10	<1
Co	91.5	149.2	106.7	116.7	165.6	176.5	190.5	130.1	119.6
Cs	3.3	6.8	6.5	3.5	2	5.4	1.7	18.5	6.3
Ga	15.7	16.8	24.6	15	15.3	28.1	29.9	18.4	16.9
Hf	6	3.2	12.4	6.7	4.3	14.7	15.2	4.6	8.6
Nb	15.1	14.5	29.1	13.9	5.4	68.9	71.3	18.6	14.5
Rb	170.4	397.7	342.6	151.7	222.8	302.6	214.1	392.9	266.2
Sn	3	8	9	4	<1	6	8	15	3
Sr	272.8	13.5	54.5	152.2	94.2	16.6	11.6	32.3	99.2
Ta	1.1	2.5	1.8	1.4	0.3	4	5.7	3.2	1.2
Th	13.3	21.8	46.8	28.7	25.4	34.4	36.2	36.6	36.3
U	1.5	5.4	5	4.1	1.8	5	6.3	8.3	1.5
V	23	<8	37	32	<8	14	9	<8	22
W	651.7	1016.8	735.1	787.4	1180.4	1331.6	1299.6	901.7	783.7
Zr	225.1	73.4	450.3	239	142.2	480.4	456.5	114.2	299.5
Y	20.5	70.3	78.2	12.9	13.4	104.5	113.1	81.5	35
La	47.9	30.6	112.9	35.9	66.4	118.4	110.9	50.8	86
Ce	105	67.6	217	113.6	118.5	243.7	237.5	98.8	159
Pr	10.31	7.91	22.98	7.5	12.21	28.38	26.91	10.91	17.35
Nd	36.8	28.1	85.1	24.2	41.4	106.4	100.3	38.9	60.9
Sm	6.48	7.7	15.77	4.15	6.47	22.88	22.41	8.66	10.41
Eu	1.27	0.22	2.53	0.74	1.54	0.41	0.45	0.63	1.62
Gd	4.99	8.48	15.24	3.13	4.95	22.72	22.34	9.43	8.52
Tb	0.7	1.8	2.36	0.49	0.63	3.72	3.66	1.86	1.21
Dy	3.99	11.93	14.31	2.89	3.22	21.88	21.54	12.38	6.62
Ho	0.7	2.44	2.88	0.6	0.51	4.16	4.44	2.72	1.28
Er	2	7.87	8.64	1.8	1.33	11.72	12.45	8.74	3.54
Tm	0.3	1.14	1.21	0.31	0.16	1.54	1.68	1.41	0.49
Yb	2.07	7.41	7.83	2.23	0.99	9.35	9.96	9.25	2.95
Lu	0.3	1.05	1.17	0.34	0.13	1.33	1.48	1.43	0.45
$(La/Yb)_N$	15.59	2.78	9.71	10.85	45.19	8.53	7.50	3.70	19.64
Eu/Eu*	0.68	0.08	0.50	0.63	0.83	0.06	0.06	0.21	0.53
T_{Zr} (W&H)	812	728	872	826	777	893	888	766	841
T_{Zr} (B)	769	675	837	790	730	869	862	721	803

report zircon saturation temperatures of 816–922 °C in the ~1.45 Ga geochemically similar granitoids in eastern CGC.

6.3. The significance of Mid-Mesoproterozoic A-type felsic plutonism in the CGC

Mukherjee et al. (2017, 2018a, 2019) demonstrate the occurrence of ~1.45 Ga A-type granitoids in a small area (the Dumka-Deoghar sector) in eastern CGC (Fig. 2a, Supplementary Figure 1). Mukherjee et al. (2018a) contend that the A-type granitoids are chemically similar to the Mid-Mesoproterozoic granitoids in Amazonia and this study shows that these granitoids are similar to the ~1.4 Ga granitoids in Laurentia (Figs. 10 and 11). The finding is unique because Mid-Mesoproterozoic felsic plutonism is largely unknown in the Greater India landmass, except for the U-Pb (zircon) ages of 1.35 Ga in the

Errakonda ferrosyenite and 1.37 Ga in the Upalapadu nepheline syenite in the east of Ongole (Kumar et al., 2007) and the neighboring 1.4 Ga Elchuru syenites (Upadhyay et al., 2006). This study demonstrates that the 1.45–1.4 Ga weakly peraluminous, ferroan, alkali calcic to calc-alkalic A-type granites with chemical signatures consistent with within-plate tectonic setting (Fig. 10) occurs in Daltongunj-Chipadohar, Simultala-Chakai, Gaya-Chatra and the Kharagpur (near Munger) Hill areas that are separated by hundreds of kilometers (Fig. 2a). Since these 1.45 Ga A-type granitoids are not reported in the adjoining crustal domains, we consider these granitoids to be exclusive to the CGC. These widespread emplacements of granitoids (occasionally garnet bearing) in central and northern CGC occur exclusive of contemporaneous mafic emplacements and mafic microgranular enclaves, and are inferred to have been derived by partial melting of biotite, K-Feldspar and plagioclase-bearing source rocks (Vielzeuf and Holloway,
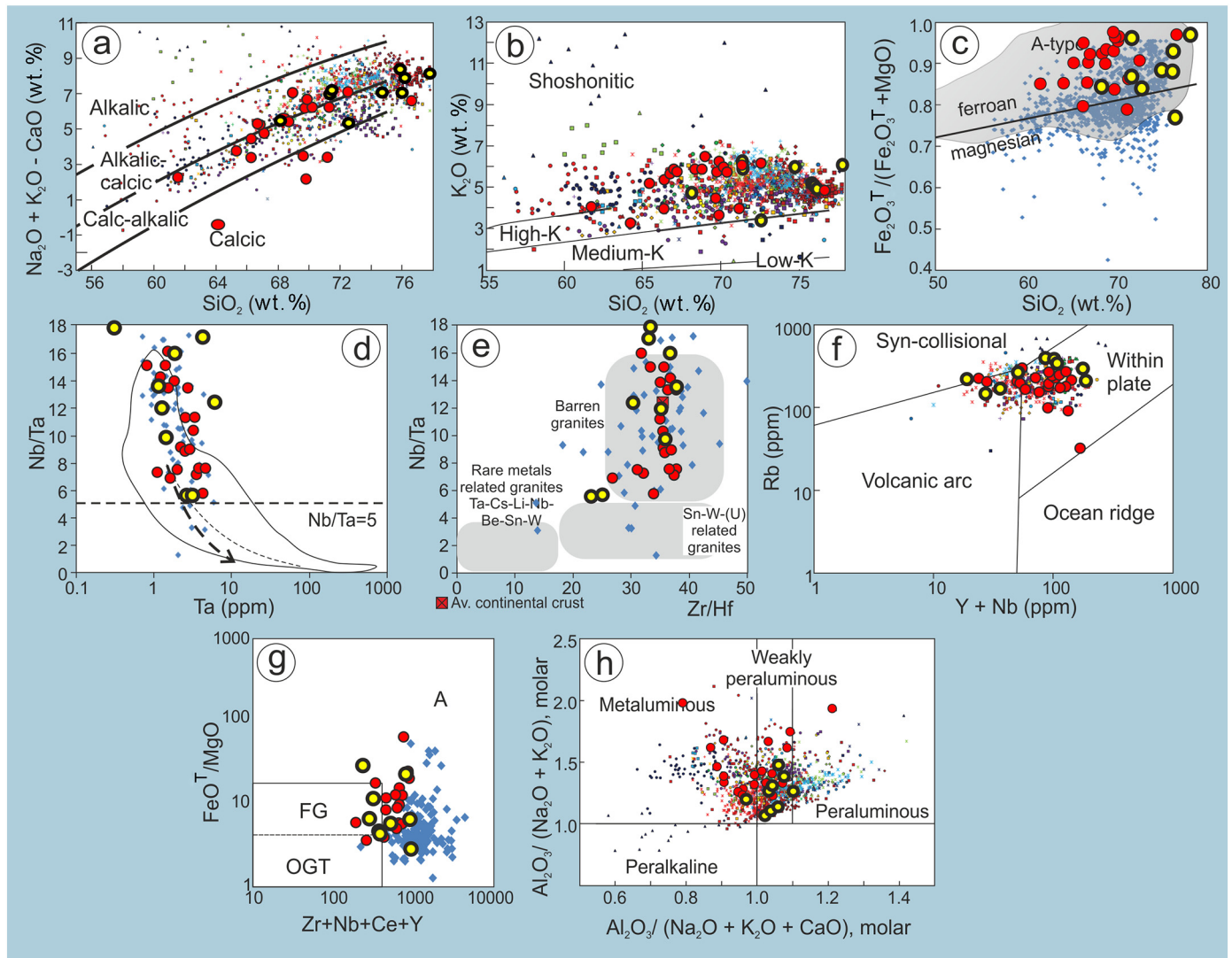
Fig. 10. Discrimination plots for the 1.45–1.4 Ga CGC granitoids from this study (filled yellow circles) and from Mukherjee et al. (2018a) (filled red circles). The data is compared with the ~1.4 Ga A-type granitoids (colored dots (a, b, f, h) (symbols given in du Bray et al., 2018), and blue dots (c–e, g)) of North America compiled by du Bray et al. (2018). Only those data of du Bray et al. (2018) that fall within the compositional range of the diagrams are shown. (a) SiO_2 versus $Na_2O + K_2O + CaO$ plot after Frost et al. (2001). (b) SiO_2 versus K_2O plot with fields from Peccerillo and Taylor (1976). (c) SiO_2 versus $Fe_2O_3^T/(Fe_2O_3^T + MgO)$ modified after Frost et al. (2001), T stands for total Fe as Fe_2O_3; gray-shaded field for A-type granitoids is adapted from Han et al. (2017); (d) Nb/Ta versus Ta plot after Ballouard et al. (2016); field shows the range of A-type granites after Ballouard et al. (2016); arrows show increasing fractionation trends computed by the authors, e.g. fractionation trends with 10 wt.% biotite + 10 wt.% muscovite + 80 wt.% (quartz) indicated by dotted line, and with 10 wt.% biotite + 10 wt.% muscovite + 0.5 wt.% ilmenite + 79.5 wt.% (quartz + feldspar) shown by broken line. (e) Nb/Ta versus Zr/Hf plots after Ballouard et al. (2016). Fields are from the authors. (f) Rb versus Y + Nb plots after Whalen et al. (1987). (g) FeO^T/MgO versus $Zr + Nb + Ce + Y$ plot after Whalen et al. (1987). (h) molar plots for $Al_2O_3/(Na_2O + K_2O + CaO)$ versus $Al_2O_3/(Na_2O + K_2O)$ after Shand (1951).

1988; Pattino-Douce and Johnston, 2001; Skjerlie and Johnston, 1993). But the heat source that produced such large volumes of granitoids should lie in the asthenosphere (Clemens, 2012). Possibly basalt under-plating due to mantle upwelling in an intra-cratonic extensional tectonic setting is the most likely scenario for the formation of these granitoids (Anderson, 1983). On the way up, the felsic magma entrained plagioclase and garnet from the source rocks (Fig. 11c).

The paucity of the 1.45–1.4 Ga monazite dates in the southern part of the CGC (Fig. 12a-left panel) could be attributed to several reasons. First, the Mid-Mesoproterozoic A-type granitoids generally lack monazites. Second, the magmatic monazites in the Mid-Mesoproterozoic A-type granitoids may have been dissolved and re-precipitated as younger (Early Neoproterozoic) grains due to accretion-related strain during the intense Early Neoproterozoic tectonism along the southern margin of CGC, where all tectonic fabrics are E-striking (Mahato et al., 2008; Rekha et al., 2011; Bhattacharya et al., 2016, 2019) and axial planar to

the prominent E–W closing D4 folds (Bhattacharya et al., 2019), and N-trending D2 fabrics, as in the Daltongunj-Chipadohar area (Fig. 5a, c), are rare, i.e. these parts of the CGC were intensely affected by the pure shear dominated transpressive deformation due to CGC-SIB accretion. And finally, U-Pb zircon age determinations from granitoids in these parts of the CGC are as yet unavailable. It is suggested, if not proven to the contrary, that the lack of ~1.4 Ga granitoids does not imply that the southern part evolved differently in the Mid Mesoproterozoic from the rest of the micro-continent.

Considerable controversy exists regarding the duration of growth of the Columbia Supercontinent, e.g. 1.9–1.5 Ga (Rogers and Santosh, 2009), 1.75–1.38 Ga (Zhang et al., 2012) and 1.65–1.58 Ga (Pisarevskiy et al., 2013). However, most authors agree that the breakup of the Supercontinent occurred between 1.45 and 1.35 Ga (Zhao et al., 2004; Rogers and Santosh, 2004, 2009; Pisarevskiy et al., 2013). This event is associated with globally widespread anorogenic felsic and
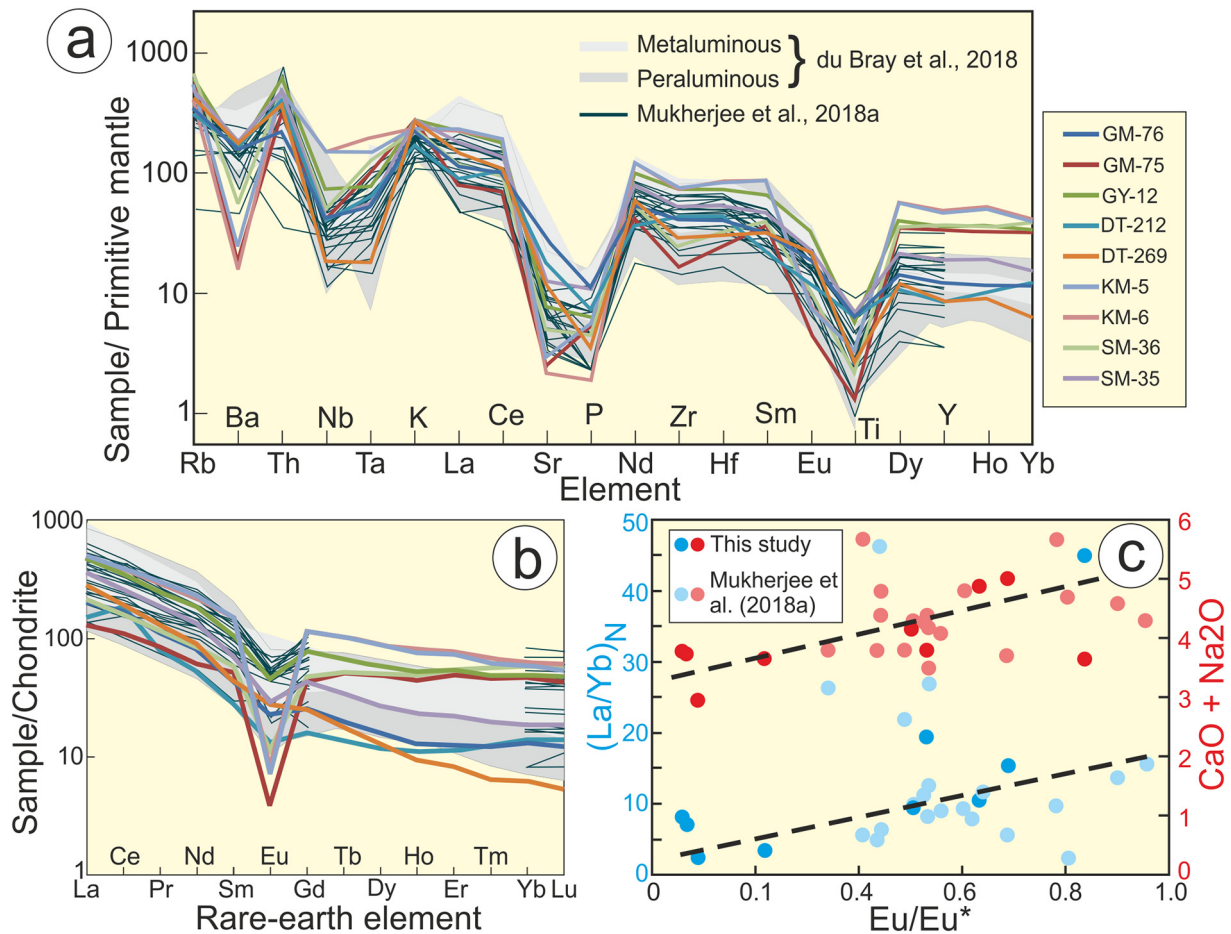
Fig. 11. (a) Trace element abundances normalized to primitive mantle (Sun and McDonough, 1989) in nine Mid-Mesoproterozoic CGC granitoids compared with ~1.4 Ga North American A-type meta- and peraluminous granitoids (compiled from du Bray et al., 2018) and ~ 1.4 Ga A-type granitoids from the CGC (compiled by Mukherjee et al., 2018a). Sample locations shown in Supplementary Figure 1. Mukherjee et al. (2018a) do not report Ho, Tm and Tb abundances in their samples. (b) Chondrite-normalized (Anders and Ebihara, 1982) rare earth element spectra in the samples compared against the North American A-type granitoids (du Bray et al., 2018) and eastern CGC granitoids (Mukherjee et al., 2018a) (c) Plots of whole rock $(La/Yb)_N$ and Eu/Eu^* versus $CaO + Na_2O$ in the CGC granitoids analyzed in this study and in Mukherjee et al. (2018a). The dotted black line is the best fit line of the data.

mafic magmatism, and intra-continental rifting and sedimentation induced by asthenospheric upwelling and/or plume-driven tectonics (Anderson, 1983; Green, 1982; Windley, 1993; Winston and Link, 1993; Frost et al., 1999, 2001; Bingen et al., 2001; Zhao et al., 2004; du Bray et al., 2018). This is especially well documented in Baltica and Amazonia forming the core of the Columbia Supercontinent, but are generally lacking in Laurentia (Hoffman, 1989) that existed prior to 1.6 Ga (Windley, 1995). The Mid Mesoproterozoic features are also exhibited in the Siberian Carton (Khudoley et al., 2001), the South China Craton (Li et al., 1996), and the Congo and Tanzania Cratons (Key and Ayres, 2000).

The widespread emplacements of 1.5–1.4 Ga A-type granitoids in the CGC that are chemically similar with the 1.45–1.32 Ga granitoids in the North American shield (Figs. 10 and 11) and Amazonia (Mukherjee et al., 2018a) suggests that the crustal block comprising the CGC prior to its accretion between the NIB and SIB within the Rodinia Supercontinent assembly experienced a distinct Mid-Mesoproterozoic phase of asthenospheric upwelling possibly related to extensional tectonism coinciding with the breakup of the >1.5 Ga Columbia Supercontinent, represented by the >1.5 Ga pre/*syn*-D1 high-grade metamorphism and anatexis in the CGC basement gneisses. It is unclear if this extensional phase led to concomitant volcanism and sediment deposition in the CGC as reported worldwide during the fragmentation of the Paleo/Mesoproterozoic supercontinent (Rogers and Santosh, 2002, 2009; Zhao et al., 2004). However, the

Mid-Mesoproterozoic (~1.35 Ga) metamorphic monazites (Fig. 12) in muscovite-biotite-garnet schists in the shallowly-dipping D3 carapace of the supracrustal unit spatially close to these granitoids in the north and central part of the CGC provides indirect evidence that some intra-crustal sedimentation may have occurred during this extensional tectonic phase: the heat source for this metamorphism may have been provided by the cooling of the ~1.4 Ga granitoids. This requires further investigation.

6.4. Early Neoproterozoic accretion in the Chottanagpur Gneiss Complex

Based on paleogeographic reconstructions, there is a consensus among researchers that India was a part of the Rodinia Supercontinent, although the position of India, central versus peripheral, in the supercontinent, is a point of debate (Zhao et al., 2004; Li et al., 2008; Meert et al., 2013; Pisarevskiy et al., 2013). The consideration that India was a part of the Rodinia assembly stems from the suggestion that the 1.1–0.9 Ga Eastern Ghats Province (EGP) (Fig. 1) comprising ultra high-T lithologies, similar and contemporaneous with, those in the Rayner Complex (Antarctica), accreted with the Greater India Landmass during the Early Neoproterozoic (Mezger and Cosca, 1999). Nasipuri et al. (2018, and references therein) contradict the suggestions based on two evidences: first, the Early Paleoproterozoic granitoids of the Bastar Craton adjacent to the western margin of the EGP (Fig. 1) experienced accretion induced anatexis at ~500 Ma, and second there is no
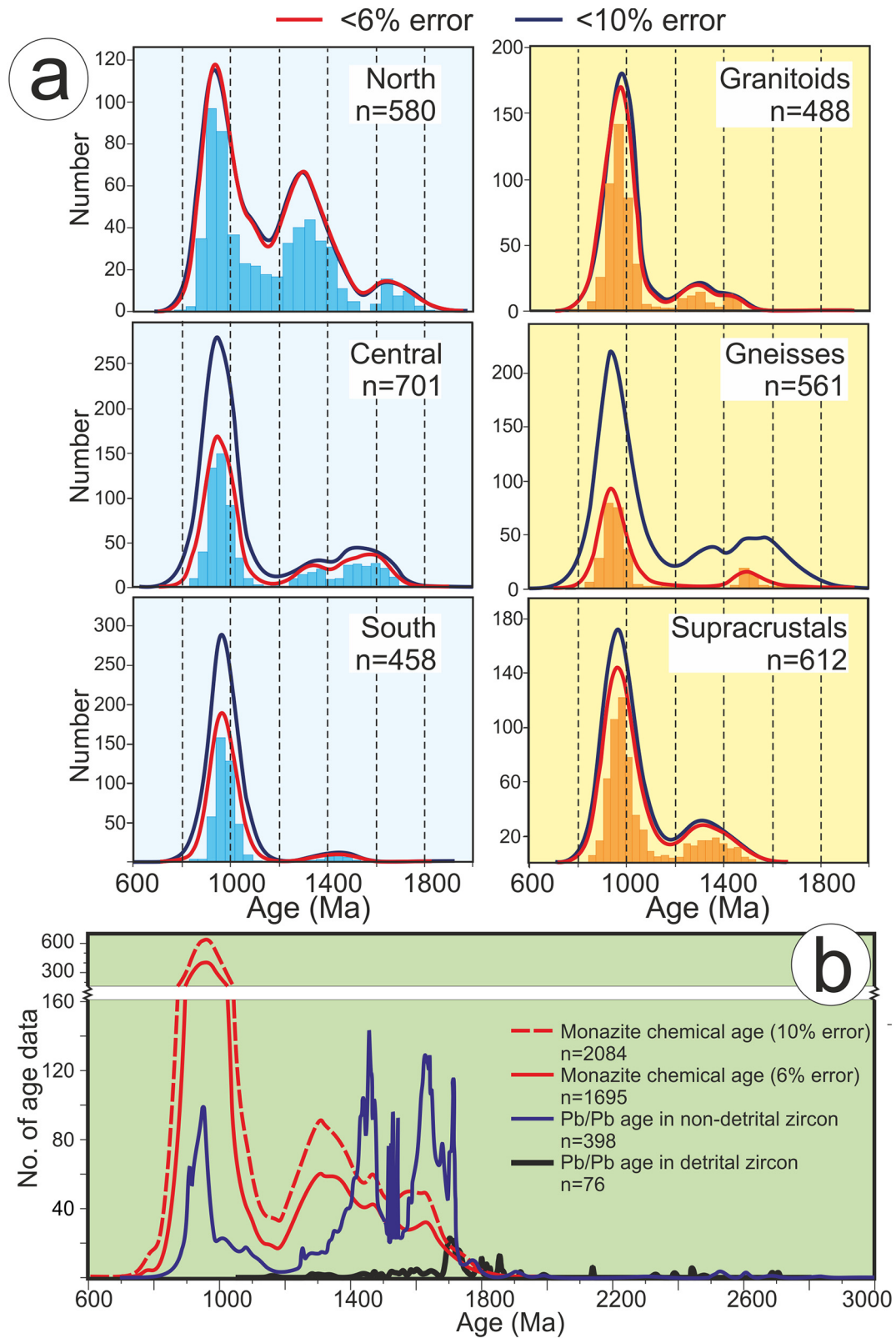
Fig. 12. (a) Panels for probability density plots of chemical dates with 6% errors (red lines, and histogram in light blue) in magmatic and metamorphic monazites the CGC are shown (this study, and see text for source of data). Probability plots with 10% errors in spot dates (deep blue lines) are shown for reference. The dates are categorized geographically (in the left panel) and lithologically (in the right panel). (b) The monazite dates with 6% and 10% errors are compared with the available (data source in text) detrital and non-detrital Pb-Pb zircons dates in the CGC.

chronological imprint of Grenvillian-age deformation-metamorphism in the craton margin juxtaposed against the EGP, which is inescapable if the ultra high-T "hot" EGP lithologies were thrust over the Bastar Craton in the Early Neoproterozoic. Nasipuri et al. (2018) suggested the EGP accretion with the Bastar Craton vis-à-vis a part of the Greater India Landmass occurred in the Pan African, ~400 Ma later during the Gondwanaland assembly.

At the eastern end of the GIPFOB, the broadly synchronous 1.0–0.9 Ga oblique accretion of the CGC between composite of the Archean Singhbhum Craton and the Mesoproterozoic North Singhbhum Mobile Belt (Mahato et al., 2008) in the south as part of the SIB (Figs. 1 and 2a), and the Gaya-Mahakoshal Belt of Paleoproterozoic granites and low-grade muscovite-biotite schists in the north as part of the NIB provides stronger evidence for the Greater Indian landmass being a part the Rodinia Supercontinent assembly. The dynamics of the subduction-accretion at the southern boundary during the Early Neoproterozoic have been established by several previous studies (Rekha et al., 2011; Bhattacharya et al., 2016, 2019; Chakraborty et al., 2019). However, this study for the first time provides U-Pb zircon dates to back up the monazite chemical dates and tectonic framework presented in Sequeira and Bhattacharya (2021) which constrains the age of the northern accretion boundary of the CGC between 0.9 and 1.0 Ga (Fig. 9h).

We have however refrained from providing possible locations of CGC in the existing reconstructions of Columbia and Rodinia Supercontinent primarily because of the lack of paleopole determinations specific to the CGC crustal block. Additionally, it is being increasingly demonstrated that the Indian landmass evolved by agglomeration of incoherently evolved crustal blocks that continued till the Pan African. During the Mid-Mesoproterozoic, the Indian sub-continent (as we see it now) did not yet exist as a single landmass, but rather, may have existed as smaller continents that amalgamated at different times along major accretion zones. Therefore, relying on paleomagnetic pole data from other crustal blocks within the Indian landmass to reconstruct the position the Chottanagpur Crustal Block within the Columbia or Rodinia Supercontinents may not be accurate.

7. Conclusions

In summary we argue that the CGC evolved as a coherently evolved crustal block (Fig. 2a–c) that (i) was possibly a part of the Columbia supercontinent (D1: >1.5 Ga high-grade metamorphism), (ii) experienced Mid-Mesoproterozoic (1.45–1.40 Ga) fragmentation that led to widespread emplacement of within-plate anorogenic granitoids (this corroborates with the findings of Mukherjee et al., 2018a, albeit from a much smaller area in east-CGC), before being (iii) finally integrated (1.0–0.9 Ga; D3-D4) into the Greater India landmass due to the oblique convergence of the NIB and the SIB (Fig. 1), coinciding with the assembly of the Rodinia supercontinent (Li et al., 2008; Evans, 2009). Thus the CGC crustal block was relocated from the Columbia Supercontinent to the Rodinia Supercontinent. The expansive Mid Mesoproterozoic within-plate A-type felsic plutonism demonstrated in this study suggests that the CGC crustal block occupied a more central position in the Columbia Supercontinent, instead of the customarily peripheral position assigned to India in the Supercontinent assembly proposed by various workers (Zhao et al., 2004; Meert and Santosh, 2017).

Appendix 1: Analytical procedures

Monazite chemical dating

Th-U-total Pb dates in monazites were determined following the methodology of Montel et al. (1996). The monazite analyses were performed using a 4-WDS CAMECA SX-100 electron probe microanalyzer in the National Facility, Indian Institute of Technology, Kharagpur. The crystal configurations, analytical conditions, and the standards for

analysis are identical to the protocol-I of Prabhakar (2013); only a brief summary is provided here. Monazite grains were analyzed using 20 kV acceleration voltage and 200 nA beam current. Synthetic standards were used to analyze REEs (LaLα, CeLα, Prβ, NdLβ, SmLα, GdLβ, DyLα, HoLβ), YLα, ThMα, UMβ, PbMα, and SiKα; natural mineral standards were used for calibrating AlKα, FeKα, PKα and CaKα. The peak-times for measurements were 10 s (Al, Si, Ca and Fe), 20 s (P) and 30 s (Y and REEs; La and Ce were analyzed for 40 s). Longer measurements were applied to PbMα (300 s), ThMα (200 s) and UMβ (200 s) spectral analyses. Background measurements were made in half the peak-time.

The element abundances, monazite spot dates and $\pm 2\sigma$ errors are presented in Supplementary Material 2. Error % for spot dates was calculated as [$100 \times \{2\sigma$ error in Ma/absolute age in Ma] following Prabhakar (2013). Spots dates with stated error % were statistically resolved for mean dates of populations using Isoplot 3.0 (Ludwig, 2012). The spot dates were monitored against the standard Moacyr monazite; the date for the Moacyr monazite is determined to be 497 ± 10 Ma (EMP age, Spear et al., 2009); 487 ± 0.5 Ma (TIMS age, Crowley et al., 2005) and 509.3 ± 0.5 Ma (TIMS age, Spear et al., 2009). The dates for the Moacyr monazite varied between 487 ± 29 Ma and 504 ± 32 Ma, with a mean value of 496 ± 8 Ma.

SIMS U-Pb (zircon) dating

The samples were crushed, and the zircon-rich fraction was obtained using heavy liquid (bromoform) and magnetic separation. The hand-picked zircon grains, under binocular microscope, in the non-magnetic fraction were arranged on double-sided adhesive tape, placed on glass slides, and covered in epoxy resin. The grains were polished till approximately half the thickness of the grains was reached. The epoxy-mounted zircon grains were then cleaned, gold coated and photographed by cathodoluminescence (CL) imaging at IIT Kharagpur (India) and UCLA. Analytical data for the samples are provided in Table 1.

The samples were analyzed in two sessions. Four samples (GY-11, GY-64, GY-68 and KM-8A) were analyzed for U-Pb-Th with the secondary ion mass spectrometer (SIMS), theCAMECA*ims*1290 ion microprobe at UCLA fitted with a Hyperion-II RF oxygen plasma source (Liu et al., 2018). The analyses were run with a mass resolving power (MRP) of ~5500. We used a ~3 nA primary beam of O_3^- ions focused to a ~5 μm spot and accelerated with a − 13 kV primary voltage to a stage held at approximately +10 kV. Two samples (DT-36 and SM-8a) were run on the CAMECA*ims*1270, with oxygen flooding, a ~ 10 nA primary beam of O^- ions focused to a ~20 μm spot, primary acceleration of −12.5 kV and stage held at +10 kV. Similar analytical protocols were followed during both sessions, the details for which are presented in Quidelleur et al. (1997). A brief summary is provided below. The following species $^{180}Hf^{16}O$, $^{94}Zr_2^{16}O$, ^{204}Pb, ^{206}Pb, ^{207}Pb, ^{208}Pb, ^{232}Th, ^{238}U, and ^{238}U ^{16}O (all of these are +1 ions.) were measured. Notably ^{235}U was not directly measured, but was calculated from ^{238}U and the terrestrial $^{235}U/^{238}U$ ratio. We used standards of known age so that we know the true $^{206}Pb/^{238}U$ ratio and can compare with the measured values to get the RSF [(true ratio)/(measured ratio)] and plot its correlation with UO/U. Unknowns were then assigned a Pb/U RSF based on their UO/U. In our sessions, we built the calibration line using FC-1 and AS3 (both 1099.1 Ma; sampled from different regions of the Duluth Gabbro complex in Minnesota, USA). The age characterization was done originally by Paces and Miller (1993). Most CAMECA ion probe laboratories use "oxygen flooding" (oxygen sprayed onto the surface of the sample for enhancing Pb's ionization) for U-Pb analyses. Using a molecular O_3^- beam compensates for this. We calculated the concentrations of Hf, Th, and U in the unknowns with reference to the 91500 zircon standard, which is homogeneous with respect to the elements. The HfO/$^{94}Zr_2$O, Th/$^{94}Zr_2$O, and U/$^{94}Zr_2$O measured for the 91500 are used to calculate an RSF for each using the known concentrations (from Wiedenbeck et al., 2004).

Major and trace element geochemistry: For whole rock geochemistry, samples weighing 2–3 kg were washed, cleaned, dried and disintegrated into cm-sized chips in a Fritsch jaw crusher. After repeated coning and quartering, ~250 g of the samples were powdered to ~200 mesh-size in a Fritsch ball mill. For major element oxide analyses, 0.25 g of the powdered samples were fused with lithium metaborate (0.75 g) and lithium tertraborate (0.5 g) at 1050 °C in Pt-crucible; and dissolved in 100 mL of 1 N HCL acid at room temperature. 5 mL of this solution was diluted to 50 mL. These solutions were analyzed using an Inductively Coupled Plasma Atomic Emission Spectroscopy (ICP-AES) in the Department of Earth Sciences, Indian Institute of Technology, Mumbai, India. The loss on ignition was determined from the % difference in weights of sample + crucible before and after firing 1.0 g of the powdered sample in a furnace up to 950 °C for 15 min in a Pt-crucible.

The samples in solution were analyzed (Table 2) for 31 trace elements (code LF100) using Lithium borate fusion and by Inductively-couple Plasma Mass spectrometry (ICP-MS) in the ACME Laboratory (Vancouver) of the Bureau Veritas Minerals (BVM). The detection limits, except for Ga, Sr and W (0.5 ppm), Ba, Be and Sn (1 ppm) and V (8 ppm), for all other rare earth elements and refractory elements are between 0.3 ppm and 0.01 ppm.

Declaration of Competing Interest

Acknowledgments

Appendix A. Supplementary data

Supplementary data to this article can be found online at https://doi.org/10.1016/j.gsf.2020.12.017.

References

Acharyya, S.K., 2003. A plate tectonic model for Proterozoic crustal evolution of Central IndianTectonic Zone. Gondwana Geol. Mag. 7, 9–31.

Anders, E., Ebihara, M., 1982. Solar-system abundances of the elements. Geochim. Cosmochim. Acta 46, 2363–2380.

Anderson, J.L., 1983. Proterozoic anorogenic granite plutonism of North America. Geol. Soc. Amer. Mem. 161, 133–154.

Anderson, I.C., Frost, C.D., Frost, B.R., 2003. Petrogenesis of the Red Mountain pluton, Laramie anorthosite complex, Wyoming: implications for the origin of A-typegranites. Precamb. Res. 124, 243–267.

Auzanneau, E., Schmidt, M.W., Vielzeuf, D., Connolly, J.A., 2010. Titanium in phengite: a geobarometer for high temperature eclogites. Contrib. Mineral. Petrol. 159, 1–24. https://doi.org/10.1007/s00410-009-0412-7.

Ballouard, C., Poujol, M., Boulvais, P., Branquet, Y., Tartèse, R., Vigneresse, J.-L., 2016. Nb-Ta fractionation in peraluminous granites: a marker of the magmatic-hydrothermal transition. Geology 44, 231–234. https://doi.org/10.1130/G37475.1.

Belica, M.E., Piispa, E.J., Meert, J.E., Pesonen, L.J., Plado, J., Pandit, M.K., Kamenov, G.D., Celestino, M., 2014. Paleoproterozoic mafic dyke swarms from the Dharwar craton; paleomagnetic poles for India from 2.37 to 1.88 Ga and rethinking the Columbia supercontinent. Precamb. Res. 244, 100–122.

Berman, R.G., 1990. Mixing properties of Ca-Mg-Fe-Mn garnets. Amer. Mineral. 75, 328–344.

Bhattacharya, A., Das, H.H., Bell, E., Chatterjee, N., Saha, L., Dutt, A., 2016. Restoration of Late Neoarchean-Early Cambrian tectonics in the Rengali orogen and its environs (eastern India): The Antarctic connection. Lithos 263, 190–212.

Bhattacharya, A., Rekha, S., Sequeira, N., Chatterjee, A., 2019. Transition from shallow to steep foliation in the Early Neoproterozoic Gangpur accretionary orogen (Eastern India): Mechanics, significance of mid-crustal deformation, and case for subduction polarity reversal? Lithos 348–349, 105196. https://doi.org/10.1016/j.lithos.2019.105196.

Bingen, B., Birkeland, A., Nordgulen, Ø., Sigmond, E.M.O., 2001. Correlation of supracrustal sequences and origin of terranes in the Sveconorwegian orogen of SW Scandinavia: SIMS data on zircon in clastic metasediments. Precamb. Res. 108, 293–318.

Boehnke, P., Watson, E.B., Trail, D., Harrison, T.M., Schmitt, A.K., 2013. Zircon saturation revisited. Chem. Geol. 351, 324–334.

Chakraborty, T., Upadhyay, D., Ranjan, S., Pruseth, K.L., Nanda, J.K., 2019. The geological evolution of the Gangpur Schist Belt, easternIndia: Constraints on the formation of the Greater Indian CFLandmass in the Proterozoic. J. Metamorph. Geol. 37, 113–151. https://doi.org/10.1111/jmg.12452.

Chatterjee, N., Ghose, N.C., 2011. Extensive Early Neoproterozoic high-grade metamorphism in North Chotanagpur Gneissic Complex of the Central Indian Tectonic Zone. Gondwana Res. 20, 362–379.

Chatterjee, N., Mazumdar, A.C., Bhattacharya, A., Saikia, R.R., 2007. Mesoproterozoic granulites of the Shillong–Meghalaya Plateau: evidence of westward continuation of the Prydz Bay Pan-African suture into Northeastern India. Precamb. Res. 152, 1–26.

Chatterjee, N., Crowley, J.L., Ghose, N.C., 2008. Geochronology of the 1.55 Ga Bengal anorthosite and Grenvillian metamorphism in the Chotanagpur gneissic complex, eastern India. Precamb. Res. 161, 303–316.

Chatterjee, N., Banerjee, M., Bhattacharya, A., Maji, A.K., 2010. Monazite chronology, metamorphism-anatexis and tectonic relevance of the mid-Neoproterozoic eastern Indian tectonic zone. Precamb. Res. 179, 99–120.

Cherniak, D.J., Watson, E.B., 2001. Pb diffusion in zircon. Chem. Geol. 172, 5–24.

Chowdhury, S., Lentz, D.R., 2011. Mineralogical and geochemical characteristics of scheelite-bearing skarns, and genetic relations between skarn mineralization and petrogenesis of the associated granitoid pluton at Sargipali, Sundergarh District, eastern India. J. Geochem. Explor. 108, 39–61.

Clemens, J.D., 2012. Granitic magmatism, from source to emplacement: a personal view. Appl. Earth Sci. 121, 107–136. https://doi.org/10.1179/1743275813Y.0000000023.

Clemens, J.D., Vielzeuf, D., 1987. Constraints on melting and magma production in the crust. Earth Planet. Sci. Lett. 86, 287–306.

Clemens, J.D., Holloway, J.R., White, A.J.R., 1986. Origin of an A-type granite: experimental constraints. Amer. Mineral. 71, 317–324.

Coggon, R., Holland, T.J.B., 2002. Mixing properties of phengitic micas and revised garnet–phengite thermobarometers. J. Metamorph. Geol. 20, 683–696.

Collins, W.J., Beams, S.D., White, A.J.R., Chappell, B.W., 1982. Nature and origin of A-Type granites with particular reference to Southeastern Australia. Contrib. Mineral. Petrol. 80, 189–200.

Condie, K.C., 2002. Breakup of a Paleoproterozoic supercontinent. Gondwana Res. 5, 41–43.

Connolly, J.A.D., 2005. Computation of phase equilibria by linear programming: a tool for geodynamic modeling and its application to subduction zone decarbonation. Earth Planet. Sci. Lett. 236, 524–541.

Corfu, F., 2013. A century of U-Pb geochronology: The long quest towards concordance. Geol. Soc. Am. Bull. 125, 33–47. https://doi.org/10.1130/b30698.1.

Creaser, R.A., Price, R.C., Wormald, R.J., 1991. A-type granites revisited: assessment of a residual-source model. Geology 19, 163–166.

Crowley, J.L., Chatterjee, N., Bowring, S.A., Sylvester, P.J., Myers, J.S., Searle, M.P., 2005. U–(Th)–Pb dating of monazite and xenotime by EPMA, LA-ICPMS, and IDTIMS: examples from Yilgarn Craton and Himalayas. 15th Annual Goldschmidt Conf. Abs. A19.

Cullers, R.L., Griffin, T., Bickford, M.E., Anderson, J.L., 1992. Origin and chemical evolution of the 1360 Ma San Isabel batholith, Wet Mountains, Colorado; a mid-crustal granite of anorogenic affinities. Geol. Soc. Am. Bull. 104, 316–328.

Dall'Agnol, R., Oliveira, D.C., 2007. Oxidized, magnetite-series, rapakivi-type granites of Carajás, Brazil: implications for classification and petrogenesis of A-type granites. Lithos 93, 215–233.

Dall'Agnol, R., Frost, C.D., Ramo, O.T., 2012. Editorial IGCP Project 510 "A-type Granites and Related Rocks through Time": Project vita, results, and contribution to granite research. Lithos 151, 1–16.

Deshmukh, T., Prabhakar, N., Bhattacharya, A., Madhavan, K., 2017. Late Paleoproterozoic clockwise P–T history in the Mahakoshal Belt, Central Indian Tectonic Zone: Implications for Columbia supercontinent assembly. Precamb. Res. 298, 56–78.

Dey, A., Mukherjee, S., Ibanez-Mejia, M., Sengupta, P., 2017. Deciphering Sedimentary Provenance and Timing of Sedimentation from a Suite of Metapelites from the Chotanagpur

Granite Gneissic Complex, India: Implications for Proterozoic Tectonics in the East-Central Part of the Indian Shield. In: Mazumder, R. (Ed.), Sediment Provenance: Influences on Compositional Change from Source to Sink. Elsevier, pp. 453–486.

Dey, A., Karmakar, S., Ibanez-Mejia, M., Mukherjee, S., Sanyal, S., Sengupta, P., 2019. Petrology and geochronology of a suite of pelitic granulites from parts of the Chotanagpur Granite Gneiss Complex, eastern India: evidence for Stenian-Tonian reworking of a late Paleoproterozoic crust. Geol. Jour. 1–30. https://doi.org/10.1002/gj.3552.

du Bray, E.A., Holm-Denoma, C.S., Lund, K., Premo, W.R., 2018. Review of the Geochemistry and Metallogeny of approximately 1.4 Ga Granitoid Intrusions of the Conterminous United States. Scientific Investigations Report 2017-5111. US Geol. Surv, Reston, Virgina, p. 44.

Evans, D.A.D., 2009. The palaeomagnetically viable, long-lived and all-inclusive Rodinia supercontinent reconstruction. Geol. Soc. Lond. Spec. Publ. 327, 371–404. https://doi.org/10.1144/SP327.16.

Evans, D.A.D., Mitchell, R.N., 2011. Assembly and breakup of the core of Paleoproterozoic-Mesoproterozoic supercontinent Nuna. Geology 39, 443–446. https://doi.org/10.1130/G31654.1.

Evans, K.V., Aleinikoff, J.D., Fanning, C.M., 2000. SHRIMP U-Pb geochronology of volcanic rocks, Belt Supergroup, western Montana: evidence for rapid deposition of sedimentary strata. Can. J. Earth Sci. 37, 1287–1300. https://doi.org/10.1139/e00-036.

Ewart, A., 1982. The mineralogy and petrology of Tertiary–recent orogenic volcanic rocks with special reference to the andesitic-basaltic compositional range. In: Thorpe, R.S. (Ed.), Andesites—Orogenic Andesites and Related Rocks. John Wiley and Sons, New York, pp. 25–87.

Ferguson, C.B., Duebendorfer, E.M., Chamberlain, K.R., 2004. Synkinematic intrusion of the 1.4 Ga Boriana Canyon Pluton, northwestern Arizona: Implications for ca. 1.4-Ga regional strain in the Western United States. J. Geol. 112, 165–183. https://doi.org/10.1086/381656.

Frost, C.D., Frost, B.R., 1997. Reduced rapakivi-type granites: the tholeiite connection. Geology 25, 647–650.

Frost, C.D., Frost, B.R., 2011. On ferroan (A-type) granitoids—their compositional variability and modes of origin. J. Petrol. 52, 39–53.

Frost, C.D., Frost, B.R., Chamberlain, K.R., Edwards, B.R., 1999. Petrogenesis of the 1.43 Ga Sherman batholith, SE Wyoming, USA: a reduced, rapakivi-type anorogenic granite. J. Petrol. 40, 1771–1802.

Frost, C.D., Bell, J.M., Frost, B.R., Chamberlain, K.R., 2001. Crustal growth by magmatic underplating–Isotopic evidence from the northern Sherman batholith. Geology 29, 515–518.

Gardes, E., Jaoul, O., Montel, J.M., Seydoux-Guillaume, A.M., Wirth, R., 2006. Pb diffusion in monazite: an experimental study of Pb + Th = 2Nd interdiffusion. Geochim. Cosmochim. Acta 70, 2325–2336.

Geological Survey of India, 2002. District Resource Map of Palamu and Garhwa, Jharkhand.

Green, T.H., 1982. Anatexis of mafic crust and high pressure crystallization of andesite. In: Thorpe, R.S. (Ed.), Andesites–Orogenic andesites and related rocks. John Wiley and Sons, New York, pp. 465–487.

Gregory, L.C., Meert, J.G., Pradhan, V., Pandit, M.K., Tamrat, E., Malone, S.J., 2006. A paleomagnetic and geochronological study of the Majhgawan Kimberlite, India: implications for the age of the Vindhyan Super Group. Precamb. Res. 149, 65–75.

Gregory, L.C., Meert, J.G., Bingen, B.H., Pandit, M.K., Torsvik, T.H., 2009. Paleomagnetic and geochronologic study of Malani Igneous suite, NW India: implications for the configuration of Rodinia and the assembly of Gondwana. Precamb. Res. 170, 13–26.

Halls, H.C., Kumar, A., Srinivasan, R., Hamilton, M.A., 2007. Paleomagnetism and U–Pb geochronology of easterly trending dykes in the Dharwar craton, India: feldspar clouding, radiating dyke swarms and the position of India at 2.37 Ga. Precamb. Res. 155, 47–68.

Han, J., Zhou, J.B., Li, L., Song, M.C., 2017. Mesoproterozoic (1.4 Ga) A-type gneissic granites in the Xilinhot terrane, NE China: first evidence for the break-up of Columbia in the eastern CAOB. Precamb. Res. 296, 20–38.

Harrison, T.M., Watson, E.B., Aikman, A.B., 2007. Temperature spectra of zircon crystallization in plutonic rocks. Geology 35, 635–638. https://doi.org/10.1130/G23505A.1.

Hazarika, P., Upadhyay, D., Pruseth, K.L., 2017. Episodic tourmaline growth and re-equilibration in mica pegmatite from the Bihar Mica Belt, India: Major- and trace-element variations under pegmatitic and hydrothermal conditions. Geol. Mag. 154, 68–86. https://doi.org/10.1017/S0016756815000916.

Hoffman, P.F., 1989. Speculations on Laurentia's first gigayear (2.0 to 1.0 Ga). Geology 17, 135–138. https://doi.org/10.1130/0091-7613(1989)017<0135:SOLSFG>2.3.CO;2.

Holland, T.J., Powell, R., 1998. An internally consistent thermodynamic data set for phases of petrological interest. J. Metamorph. Geol. 16, 309–343. https://doi.org/10.1111/j.1525-1314.1998.00140.x.

Holland, T., Powell, R., 2001. Calculation of phase relations involving Haplogranitic melts using an internally consistent thermodynamic dataset. J. Petrol. 42, 673–683. https://doi.org/10.1093/petrology/42.4.673.

Hoskin, P.W.O., Schaltegger, U., 2003. The composition of zircon and igneous and meta-morphic petrogenesis. Rev. Mineral. Geochem. 53, 27–62.

Huang, H.Q., Li, X.H., Li, W.X., Li, Z.X., 2011. Formation of high $\delta^{18}O$ fayalite-bearing A type granite by high-temperature melting of granulitic metasedimentary rocks, southern China. Geology 39, 903–906.

Karmakar, S., Bose, S., Sarbadhikari, A.B., Das, K., 2011. Evolution of granulite enclaves and associated gneisses from Purulia, Chhotanagpur Granite Gneiss complex, India: evidence for 990–940Ma tectonothermal event(s) at the eastern India cratonic fringe zone. J. Asian Earth Sci. 41, 69–88.

Kemp, A.I.S., Wormald, R.J., Whitehouse, M.J., Price, R.C., 2005. Hf isotopes in zircon reveal contrasting sources and crystallization histories for alkaline to peralkaline granites of Temora, southeastern Australia. Geology 33, 797–800.

Key, R.M., Ayres, N., 2000. The 1998 edition of the National Geological Map of Botswana. J. African Earth Sci. 30, 427–451.

Khudoley, A.K., Rainbird, R.H., Stern, R.A., Kropachev, A.P., Heaman, L.M., Zanin, A.M., Podkovyrov, V.N., Belova, V.N., Sukhorukov, V.I., 2001. Sedimentary evolution of the Riphean–Vendian basin of southeastern Siberia. Precamb. Res. 111, 129–163.

King, P.L., Chappell, B.W., Allen, C.M., White, A.J.R., 2001. Are A-type granites the high temperature felsic granites? Evidence from fractionated granites of the Wangrah suite. Australian J. Earth Sci. 48, 501–514.

Kirkland, C.L., Smithes, R.H., Taylor, R.J.M., Evans, N., McDonald, B., 2015. Zircon Th/U ratios in magmatic environs. Lithos 212–215, 397–414.

Kumar, K.V., Frost, C.D., Frost, B.R., Chamberlain, K.R., 2007. The Chimakurti, Errakonda, and Uppalapadu plutons, Eastern Ghats Belt, India: an unusual association of tholeiitic and alkaline magmatism. Lithos 97, 30–57. https://doi.org/10.1016/j.lithos.2006.11.008.

Le Maitre, R.W., 1989. A Classification of Igneous Rocks and Glossary of Terms. Oxford, United Kingdom, Blackwell Scientific, p. 193.

Li, Z.X., Zhang, L., Powell, C.M.A., 1996. Positions of the East Asian cratons in the Neoproterozoic Supercontinent Rodinia. Australian J. Earth Sci. 43, 593–604.

Li, Z.X., Bogdanova, S.V., Collins, A.S., Davidson, A., De Waele, B., Ernst, R.E., Fitzsimons, I.C.W., Fuck, R.A., Gladkochub, D.P., Jacobs, J., Karlstrom, K.E., Lu, S., Natapov, L.M., Pease, V., Pisarevsky, S.A., Thrane, K., Vernikovsky, V., 2008. Assembly, configuration, and break-up history of Rodinia: a synthesis. Precamb. Res. 160, 179–210.

Linnemann, U., Ouzegane, K., Drareni, A., Hofmann, M., Becker, S., Gärtner, A., Sagawe, A., 2011. Sands of West Gondwana: Anarchive of secular magmatism and plate interactions–A casestudy from the Cambro–Ordovician section of the Tassili OuanAhaggar (Algerian Sahara) using U–Pb–LA-ICP-MS detritalzircon ages. Lithos 123, 188–203.

Liu, M.C., McKeegan, K.D., Harrison, T.M., Jarzebinski, G., Vltava, L., 2018. The Hyperion-II radio-frequency oxygen ion source on the UCLA ims1290 ion microprobe: Beam characterization and applications in geochemistry and cosmochemistry. Int. J. Mass Spectrom. 424, 1–9.

Ludwig, K.R., 2012. Isoplot/Ex version 4.15, a geochronological toolkit for Microsoft Excel. Berkeley Geochronology Center Spec. Pub. 4, p. 78.

Mahato, S., Goon, S., Bhattacharya, A., Mishra, B., Bernhardt, H.-J., 2008. Thermo-tectonic evolution of the North Singhbhum Mobile Belt (eastern India): a view from the western part of the belt. Precamb. Res. 162, 102–127.

Maji, A.K., Goon, S., Bhattacharya, A., Mishra, B., Mahato, S., Bernhardt, H.J., 2008. Proterozoic polyphase metamorphism in the Chhotanagpur Gneissic Complex (India), and implication for trans-continental Gondwanaland correlation. Precamb. Res. 162, 385–402.

Malone, S.J., Meert, J.G., Banerjee, D.M., Pandit, M.K., Tamrat, E., Kamenov, G.D., Pradhan, V.R., Sohl, L.E., 2008. Paleomagnetism and detrital zircon geochronology of the Upper Vindhyan sequence, Son Valley and Rajasthan, India: a ca. 1000 Ma closure age for the Purana basins? Precamb. Res. 164, 137–159.

Manikyamba, C., Kerrich, R., 2011. Geochemistry of alkaline basalts and associated high-Mg basalts from the 2.7 Ga Penakacherla Terrane, Dharwar Craton, India: an Archean depleted mantle-OIB array. Precamb. Res. 188, 104–122.

Mattinson, J.M., Graubard, C.M., Parkinson, D.L., McClelland, W.C., 1996. U-Pb Reverse Discordance in Zircons: The Role of Fine-Scale Oscillatory Zoning and Sub-Micron Transport of Pb. Earth Processes: Reading the Isotopic Code. Am Geophys Union, Geophys Monogr, pp. 355–370.

McMenamin, M.A.S., McMenamin, D.L.S., 1990. The Emergence of Animals: The Cambrian Breakthrough. Columbia University Press, New York, p. 217.

Meert, J.G., Santosh, M., 2017. The Columbis supercontinent revisited. Gondwana Res. 50, 67–83. https://doi.org/10.1016/j.gr.2017.04.011.

Meert, J.G., Manoj, M.K., Kamenov, G.D., 2013. Further geochronological and paleomagnetic constraints on Malani (and pre-Malani) magmatism in NW India. Tectonophysics 608, 1254–1267.

Mezger, K., Cosca, M., 1999. The thermal history of the eastern Ghats Belt (India), as revealed by U–Pb and $^{40}Ar/^{39}Ar$ dating of metamorphic and magmatic minerals: Implications for the SWEAT hypothesis. Precamb. Res. 94, 251–271. https://doi.org/10.1016/S0301-9268(98)00118-1.

Miller, K.C., Hargraves, R.B., 1994. Paleomagnetism of some Indian kimberlites and lamproites. Precamb. Res. 69, 259–267.

Miller, C.F., McDowell, S.M., Mapes, R.W., 2003. Hot and cold granites: Implications of zircon saturation temperatures and preservation of inheritance. Geology 31, 529–532.

Montel, J.M., Foret, S., Veschambre, M., Nicollet, C., Provost, A., 1996. Electron microprobe dating of monazite. Chem. Geol. 131, 37–53.

Mukherjee, S., Dey, A., Sanyal, S., Ibanez-Mejia, M., Dutta, U., Sengupta, P., 2017. Petrology and U–Pb geochronology of zircon in a suite of charnockitic gneisses from parts of the Chotanagpur Granite Gneiss Complex (CGGC): Evidence for the reworking of a Mesoproterozoic basement during the formation of the Rodinia supercontinent. In: Pant, N.C., Dasgupta, S. (Eds.), Crustal Evolution of India and Antarctica: The Supercontinent Connection. Geol. Soc. London Spec. Pub 457, pp. 197–232.

Mukherjee, S., Dey, A., Ibanez-Mejia, M., Sanyal, S., Sengupta, P., 2018a. Geochemistry, U-Pb geochronology and Lu-Hf isotope systematics of a suite of ferroan (A-type) granitoids from the CGGC: evidence for Mesoproterozoic crustal extension in the East India shield. Precamb. Res. 305, 40–63. https://doi.org/10.1016/j.precamres.2017.11.018.

Mukherjee, S., Dey, A., Sanyal, S., Sengupta, P., 2018b. Tectonothermal imprints in a suite of mafic dykes from the Chotanagpur Granite Gneissic complex (CGGC), Jharkhand, India: evidence for late Tonian reworking of an early Tonian continental crust. Lithos 320–321, 490–514. https://doi.org/10.1016/j.lithos.2018.09.014.

Mukherjee, S., Dey, A., Sanyal, S., Ibanez-Mejia, M., Sengupta, P., 2019. Bulk rock and zircon geochemistry of granitoids from the Chotanagpur Granite Gneissic Complex (CGGC): implications for the late Paleoproterozoic continental arc magmatism in the East Indian Shield. Contrib. Mineral. Petrol. 174, 67. https://doi.org/10.1007/s00410-019-1601-7.

Nagaraju, E., Parashuramulub, V., Kumar, A., Srinivas Sarma, D., 2018. Paleomagnetism and geochronological studies on a 450km long 2216Ma dyke from the Dharwar craton, southern India. Physics Earth Planet. Int. 274, 222–231.

Nasipuri, P., Corfu, A., Bhattacharya, A., 2018. Eastern Ghats Province (India)–Rayner Complex (Antarctica) accretion: timing the event. Lithosphere 10, 523–529. https://doi.org/10.1016/j.pepi.2017.11.006.

Nyman, M.W., Karlstrom, K.E., Kirby, E., Graubard, C.M., 1994. Mesoproterozoic contractional orogeny in western North America: evidence from ca. 1.4 Ga plutons. Geology 22, 901–904.

Oliveira, D.C., Dall'Agnol, R., Barros, C.E.M., Oliveira, M.A., 2009. Geology, geochemistry and magmatic evolution of the Paleoproterozoic, anorogenic oxidized A-type Redenção granite of the Jamon Suite, eastern Amazonian Craton, Brazil. Can. Mineral. 47, 1441–1468.

Paces, J.B., Miller, J.D., 1993. Precise U-Pb ages of Duluth Complex and related mafic intrusions, northeastern Minnesota: Geochronological insights to physical, petrogenetic, paleomagnetic, and tectonomagmatic processes associated with the 1.1 Ga Midcontinent Rift System. J. Geophys. Res. 98, 13997–14013. https://doi.org/10.1029/93JB01159.

Patel, S.C., Sundararaman, S., Dey, R., Thakur, S.S., Kumar, M., 2007. Deformation Pattern in a Proterozoic Low Pressure Metamorphic Belt near Ramanujganj, Western Chhotanagpur Terrane. J. Geol. Soc. India 70, 207–216.

Pattino-Douce, A.E., Johnston, A.D., 2001. Phase equilibria and melt productivity in the pelitic system: implications for the origin of peraluminous granitoids and aluminous granulites. Contrib. Mineral. Petrol. 107, 202–218. https://doi.org/10.1007/BF00310707.

Peccerillo, A., Taylor, S.R., 1976. Geochemistry of Eocene calc-alkaline volcanic rocks from the Kastamonu area, Northern Turkey. Contrib. Mineral. Petrol. 58, 63–81.

Pisarevskiy, S.A., Biswal, T.K., Xuan-Ce Wang, B.C., De Waele, B.E., Ernst, R., Ulf Söderlund, U.H., Tait, J.A., Ratre, K., Singh, Y.K., Cleve, M., 2013. Palaeomagnetic, geochronological, and geochemical study of Mesoproterozoic Lakhna Dykes in the Bastar Craton, India: implications for the Mesoproterozoic supercontinent. Lithosphere 174, 125–143.

Pivarunasa, A.F., Meert, J.G., Pandit, M.K., Sinha, A., 2019. Paleomagnetism and geochronology of mafic dykes from the Southern Granulite Terrane, India: Expanding the Dharwar craton southward. Tectonophysics 760, 4–22. https://doi.org/10.1016/j.tecto.2018.01.024.

Poitrasson, F., Chenery, S., Shephard, T.J., 2000. Electron microprobe and LA-ICP-MS study of monazite hydrothermal alteration: implications for U–Th–Pb geochronology and nuclear ceramics. Geochim. Cosmochim. Acta 64, 3283–3297.

Powell, R., Holland, T.J.B., 1999. Relating formulations of the thermodynamics of mineral solid solutions; activity modeling of pyroxenes, amphiboles and micas. Amer. Mineral. 84, 1–14.

Prabhakar, N., 2013. Resolving poly-metamorphic Paleoarchean ages by chemical dating of monazites using multi-spectrometer U, Th and Pb analyses and sub-counting methodology. Chem. Geol. 347, 255–270.

Prabhakar, N., Bhattacharya, A., 2013. Paleoarchean partial convective overturn in the Singhbhum Craton, Eastern India. Precambrian Res. 231, 106–121.

Prabhakar, N., Bhattacharya, A., Sathyanarayanan, M., Mukherjee, P., 2014. Structural, petrological, and chronological constraints from Eastern India and implications for the ~1.0 Ga assembly of Greater India. J. Geol. 122, 411–432. https://doi.org/10.1086/676459.

Pradhan, V.R., Meert, J.G., Pandit, M.K., Kamenov, G., Gregory, L.C., Malone, S.J., 2010. India's changing place in global Proterozoic reconstructions: new geochronologic constraints on key paleomagnetic poles from the Dharwar and Aravalli/Bundelkhand cratons. J. Geodynamics 50, 224–242.

Pradhan, V.R., Meert, J.G., Pandit, M.K., Kamenov, G., Mondal, Md.E.A., 2012. Paleomagnetic and geochronological studies of the mafic dykeswarms of Bundelkhand craton, Central India: Implications for the tectonic evolution and paleogeographic reconstructions. Precamb. Res. 198–199, 51–76.

Quidelleur, X., Grove, M., Harrison, T.M., Yin, A., Ryerson, F.J., 1997. Thermal evolution and slip history of Renbu Zedong thrust, southeastern Tibet. J. Geophys. Res. 102, 2659–2679.

Radhakrishna, B.P., Naqvi, S.M., 1986. Precambrian continental crust of India and its evolution. J. Geol. 94, 145–166.

Radhakrishnan, T., Mathew, J., 1996. Late Precambrian (850–800 Ma) palaeomagnetic pole for the South Indian shield from the Harohalli alkaline dykes: geotectonic implications for Gondwana reconstructions. Precamb. Res. 80, 77–87.

Rasmussen, B., Muhling, J.R., 2007. Monazite begets monazite: evidence for dissolution of detrital monazite and reprecipitation of syntectonic monazite during low-grade regional metamorphism. Contrib. Mineral. Petrol. 154, 675–689.

Rekha, S., Upadhyay, D., Bhattacharya, A., Kooijman, E., Goon, S., Mahato, S., Pant, N.C., 2011. Lithostructural and chronological constraints for tectonic restoration of Proterozoic accretion in the Eastern Indian Precambrian shield. Precamb. Res. 187, 313–333.

Rogers, J.J.W., Santosh, M., 2002. Configuration of Columbia, a Mesoproterozoic supercontinent. Gondwana Res. 5, 5–22.

Rogers, J.J.W., Santosh, M., 2004. Continents and Supercontinents. Oxford University Press, Oxford, p. 298.

Rogers, J.J.W., Santosh, M., 2009. Tectonics and surface effects of the supercontinent Columbia. Gondwana Res. 15, 373–380.

Rubatto, D., 2002. Zircon trace element geochemistry; partitioning with garnet and the link between U–Pb ages and metamorphism. Chem. Geol. 184, 123–138.

Rudnick, R.L., Fountain, D.M., 1995. Nature and composition of the continental crust: a lower crustal perspective. Rev. Geophys. 33, 267–309.

Saikia, A., Gogoi, B., Kaulina, T., Lialina, L., Bayanova, T., Ahmad, M., 2017. Geochemical and U–Pb zircon age characterization of granites of the Bathani Volcano Sedimentary sequence, Chotanagpur Granite Gneiss Complex, eastern India: vestiges of the Nuna supercontinent in the Central Indian Tectonic Zone. Geol. Soc. London Spec. Pub. 457. https://doi.org/10.1144/SP457.11.

Santosh, M., Morimoto, R., Tsutsumi, Y., 2006. Geochronology of the khondalite belt of Trivandrum Block, Southern India: Electron probe ages and implications for Gondwana tectonics. Gondwana Res. 9, 261–278. https://doi.org/10.1016/j.gr.2005.11.003.

Sarkar, A.N., Basu Mallick, S., 1982. Study of palaeodynamics inthe Rajgir metasedimentary belt, Bihar: stress system crustal shortening and deformation patterns. Rec. Geol. Surv. India 112, 25–32.

Sequeira, N., 2020. Tectonics of the Precambrian crystalline rocks of the Chottanagpur Gneiss Complex (eastern India), and implications for global correlations. Unpublished PhD thesis. Indian Institute of Tecnology, Kharagpur, p. 248.

Sequeira, N., Bhattacharya, A., 2020. Early Neoproterozoic deformation kinematics in the Chottanagpur Gneiss Complex: Evidence from the curvilinear Falls Shear Zone, eastern India. Lithosphere https://doi.org/10.2113/2020/8820919.

Sequeira, N., Bhattacharya, A., 2021. Early Neoproterozoic accretion at the northern margin of the Chottanagpur Gneiss Complex (India), and correlation with Western Australia Proterozoic belts (under revision).

Sequeira, N., Mahato, S., Rahl, J., Sarkar, S., Bhattacharya, A., 2020. The anatomy and origin of a syn-convergent Grenvillian-age metamorphic core complex, Chottanagpur Gneiss Complex, Eastern India. Lithosphere https://doi.org/10.2113/2020/8833404.

Shand, S.J., 1951. Eruptive Rocks. John Wiley, New York, p. 488.

Skjerlie, K.P., Johnston, A.D., 1993. Fluid-absent melting behavior of an F-rich tonalitic gneiss at mid-crustal pressures—Implications for the generation of anorogenic granites. J. Petrol. 34, 785–815.

Spear, F.S., Pyle, J.M., Cherniak, D., 2009. Limitations of chemical dating of monazite. Chem. Geol. 266, 218–230.

Spencer, C.J., Kirkland, C.L., Taylor, R.J.M., 2016. Strategies towards statistically robust interpretations of in situ U–Pb zircon geochronology. Geosci. Front. 7, 581–589. https://doi.org/10.1016/j.gsf.2015.11.006.

Stepanov, A., Mavrogenes, J.A., Meffre, S., Davidson, P., 2014. The key role of mica during igneous concentration of tantalum. Contrib. Mineral. Petrol. 167, 1009–1016. https://doi.org/10.1007/s00410-014-1009-3.

Sun, S., McDonough, W.F., 1989. Chemical and isotopic systematics of oceanic basalts: implications for mantle composition and processes. Geol. Soc. London 42, 313–345. https://doi.org/10.1144/GSL.SP.1989.042.01.19.

Torsvik, T.H., Carter, L.M., Ashwal, L.D., Bhushan, S.K., Pandit, M.K., Jamtveit, B., 2001. Rodinia refined or obscured: palaeomagnetism of the Malani igneous suite (NW India). Precamb. Res. 108, 319–333.

Turner, S.P., Foden, J.D., Morrison, R.S., 1992. Derivation of some A-type magmas by fractionation of basaltic magma: an example from the Padthaway ridge, South Australia. Lithos 28, 151–179.

Upadhyay, D., Raith, M., Mezger, K., Hammerschmidt, K., 2006. Mesoproterozoic rift-related alkaline magmatism at Elchuru, Prakasam Alkaline Province, SE India. Lithos 89, 447–477.

Vielzeuf, D., Holloway, J.R., 1988. Experimental determination of the fluid-absent melting relations in the pelitic system. Contrib. Mineral. Petrol. 98, 257–276.

Watson, E.B., Harrison, T.M., 1983. Zircon saturation revisited: temperature and composition effects in a variety of crustal magma types. Earth Planet. Sci. Lett. 64, 295–304.

Whalen, J.B., Currie, K.L., Chappell, B.W., 1987. A-type granites: Geochemical characteristics, discrimination and pedogenesis. Contrib. Mineral Petrol. 95, 407–419.

White, L., Ireland, T., 2012. High-uranium matrix effect in zircon and its implications for SHRIMP U-Pb age determinations. Chem. Geol. 306/307, 78–91. https://doi.org/10.1016/j.chemgeo.2012.02.025.

White, R.W., Powell, R., Holland, T.J.B., 2001. Calculation of partial melting equilibria in the system Na2O–CaO–K2O–FeO–MgO–Al2O3–SiO2–H2O (NCKFMASH). J. Metamorph. Geol. 19, 139–153.

Wiedenbeck, M., 1995. An example of reverse discordance during ion microprobe zircon dating: An artifact of enhanced ion yields from a radiogenic labile Pb. Chem. Geol. 125, 197–218. https://doi.org/10.1016/0009 -2541(95)00072-T.

Wiedenbeck, M., Hanchar, J.M., Peck, W. H., Sylvester, P., Valley, J., Whitehouse, M., Kronz, A., Morishita, Y., Nasdala, L., Fiebig, J., Franchi, I., Girard, J.-P., Greenwood, R.C., Hinton, R., Kita, N., Mason, P.R.D., Norman, M., Ogasawara, M., Piccoli, P.M., Rhede, D., Satoh, H., Schulz-Dobrick, B., Skår, Ø., Spicuzza, M.J., Terada, K., Tindle, A., Togashi, S., Vennemann, T., Xie, Q. Zheng, Y.-F., 2004. Further characterization of the 91500 zircon crystal. Geostand. Geoanal. Res. 28, 9–39.

Williams, I.S., Claesson, S., 1987. Isotopic evidence for the Precambrian provenance and Caledonian metamorphism of high grade paragneisses from the Seve Nappes,Scandinavian Caledonides: II. Ion microprobe zircon U–Th–Pb. Contrib. Mineral. Petrol. 97, 205–217.

Windley, B.F., 1993. Proterozoic anorogenic magmatism and its orogenic connections. J. Geol. Soc. London 150, 39–50.

Windley, B.F., 1995. The Evolving Continents. Third edition. Wiley, Chichester, p. 526.

Winston, D., Link, P.K., 1993. Middle Proterozoic rocks of Montana, Idaho and eastern Washington: the Belt Supergroup. In: Reed, J.C., Jr Bickford, M.E., Houston, R.S., Link, P.K., Rankin, R.W., Sims, P.K., Van Schmus, W.R. (Eds.), Precambrian: Conterminous U.S., C-2. Geol. Soc. Amer. (Boulder), pp. 487–517.

Worrall, F., Pearson, D.G., 2001. Water-rock interaction in an acidic mine discharge as indicated by rare earth element patterns. Geochim. Cosmochim. Acta 65, 3027–3040. https://doi.org/10.1016/S0016-7037(01)00662-7.

Yakymchuk, C., Kirkland, C.L., Clark, C., 2018. Th/U ratios in metamorphic zircon. J. Metamorph. Geol. 36, 715–737. https://doi.org/10.1111/jmg.12307.

Zhang, X.H., Yuan, L.L., Xue, F.H., Zhang, Y., 2012. Contrasting Triassic ferroan granitoids from northwestern Liaoning, North China: magmatic monitor of Mesozoic decratonization and craton–orogen. Lithos 144–145, 12–23.

Zhao, G., Sun, M., Wilde, S.A., Li, S., 2004. A Paleo-Mesoproterozoic supercontinent: assembly, growth and breakup. Earth-Sci. Rev. 67, 91–123.